

UCSF

UC San Francisco Electronic Theses and Dissertations

Title

Role of cell identity in growth cone extension during Drosophila visual circuit development

Permalink

<https://escholarship.org/uc/item/26q7v974>

Author

Ji, Weiyue

Publication Date

2021

Peer reviewed|Thesis/dissertation

Role of cell identity in growth cone extension during *Drosophila* visual circuit development

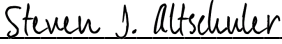
by
Weiyue Ji

DISSERTATION
Submitted in partial satisfaction of the requirements for degree of
DOCTOR OF PHILOSOPHY

in
Biophysics

in the
GRADUATE DIVISION
of the
UNIVERSITY OF CALIFORNIA, SAN FRANCISCO

Approved:

DocuSigned by:

3BE37B146DB5437... Steven J. Altschuler
Chair

DocuSigned by:

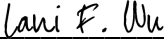
499... Thomas R. Clandinin

DocuSigned by:

499... Graeme Davis

DocuSigned by:

4A3... Orion Weiner

DocuSigned by:

16... Lani F. Wu
Committee Members

Acknowledgements

First, I would like to thank my mentors, Steven Altschuler and Lani Wu, for welcoming me as one of their first graduate students in UCSF and guiding me through the journey of scientific discovery. The *Drosophila* visual circuit is such a beautiful yet complex system, and I am grateful that they allowed me to go after this exciting problem and provided all the tools that helped me in my pursuit. I am also very thankful for their help with my professional development from a fresh college graduate to a young scientist.

I would also like to thank my qualifying exam and thesis committee members, Benjamin Cheyette, Patrick O'Farrell, Michael Stryker, Thomas Clandinin, Graeme Davis, and Orion Weiner. I really appreciated their tremendous help in developing my thesis proposal, prioritizing projects, troubleshooting experiments, and preparing the manuscript for publication. In addition, I would like to thank Peter Robin Hiesinger and Claude Desplan for their helpful suggestions during the development of the project, and Raul Andino for allowing us to share working space with his fly team.

I would also like to thank all past and current members of the Altschuler-Wu lab for their help in my development as a scientist. I have learned so much from each one of them. Especially, I would like to thank Marion Langen for her scientific guidance, thoughtful advice, and patience. I would also like to thank my fellow graduate student comrades in the lab. Thank you, Leanna Morinishi and Ina Chen, my fellow iPQbers who joined the lab at the same time, for going through the ups and downs of graduate school together; and thank you, Chris Waters, for all the midnight science discussions and life complaints.

And in the end, I would like to thank all my friends and family for being there with me for the past seven years.

To my parents, thank you so much for your unconditional support with me pursuing graduate study across the globe and 15-hours apart. Although I could only go back home twice throughout my entire time in graduate school, your love and care have always surrounded me here in San Francisco.

To Zairan, my labmate/schoolmate/roommate, and the witness of my online wedding, I am blessed to have you as my friend for almost ten years from Beijing to San Francisco, and I hope we can continue

exploring this “foreign” nation together. To Rui and Handuo, my iGEM buddies, our lives and scientific journeys have always felt so close together even though we are physically continent apart. To Zhou, my childhood friend since middle school, I am so glad that our life path converged again in the Bay Area for the past two years, and we were able to explore some of the great food that this area has to offer together, albeit physical distance never weakened our friendship.

Finally, to Yufeng, my partner: From my qualifying exam to my final year, you’ve experienced graduate school together with me. Thank you for all you have done for me, from cooking late-night dinner while I am busy with experiments, to enduring my complaints and ill tempers during rough research times. I cannot imagine life without you for the past five years and I am thrilled to begin the next chapter of our lives together.

Acknowledgements of previously published materials and research contributions

Chapter 1 of this dissertation is unpublished. Weiyue Ji wrote the chapter and created all the figures.

Chapter 2 of this dissertation was previously published. The text in Chapter 2 is a reprint and expansion of the materials as it appears on BioRxiv (<https://doi.org/10.1101/2020.10.13.337865>). Steven J. Altschuler and Lani F. Wu supervised the research that forms the basis of this chapter and were involved in the writing process. The primary data generation and analysis was performed by Weiyue Ji who also wrote the manuscript and created all tables and figures.

Contributions

Chapter 2:

Weiyue Ji, Lani F. Wu, Steven J. Altschuler. On the role of photoreceptor identity in controlling accurate wiring of the *Drosophila* visual circuit. bioRxiv 2020.10.13.337865; doi:

<https://doi.org/10.1101/2020.10.13.337865>

Role of cell identity in growth cone extension during *Drosophila* visual circuit development

Weiyue Ji

Abstract

The formation of repeated patterns is a recurring theme during tissue development. Well-studied models include the pigmentation of fish skins, the spacing and orientation of hair follicles, and the connection of sensory neurons. How do seemingly complex, yet highly organized patterns emerge? What rules underlie the development of these cellular patterns? A major challenge is to uncover rules in the face of “biological noise”, arising from stochastic variability of individual cells, local warping of the developing tissue, and specimen-to-specimen differences.

Here, I investigated rules governing neuronal pattern formation in the context of *Drosophila* visual circuit development, where the outer photoreceptors, R1-R6, resort in the lamina layer of the brain to form the stereotyped neural superposition (NSP) circuit. To hunt for signals within the biological noise, I developed a data-driven, standardized coordinate system to characterize the ensemble behaviors of photoreceptors. With this, I was able to identify rules that govern cell-type-specific extension velocities of the photoreceptor pair R3/R4, which uniquely exhibit asymmetric targeting. Specifically, I found that the extension speeds of the R3 and R4 growth cones are inherent to their cell identities. Further, to showcase the predictive power of the coordinate system, I made a computational prediction that extension angles can be explained by a weighted nearest-neighbor repulsion model. My work provides a new case study of how pattern formation rules — hidden within phenotypic variability — can be inferred by quantitative analysis during the development of living organisms.

Table of Contents

CHAPTER 1 : BACKGROUND	1
INTRODUCTION	2
PHOTORECEPTOR DIFFERENTIATION IN THE EYE IMAGINAL DISK.....	3
PHOTORECEPTOR AXON PATHFINDING TO THE LAMINA	4
PHOTORECEPTOR RESORTING IN THE LAMINA	5
LAMINA CARTRIDGE AND SYNAPSE FORMATION.....	6
SUMMARY.....	6
REFERENCES.....	11
 CHAPTER 2 : ANALYSIS OF GROWTH CONE EXTENSION IN STANDARDIZED COORDINATES	
 HIGHLIGHTS SELF-ORGANIZATION RULES DURING WIRING OF THE <i>DROSOPHILA</i> VISUAL SYSTEM ...	17
ABSTRACT	18
INTRODUCTION	19
RESULTS	19
<i>Changes in R3 or R4 cell identity lead to changes in final targeting</i>	<i>19</i>
<i>Wild-type R3s and R4s exhibit asymmetric speeds but symmetric directions of extension</i>	<i>21</i>
<i>Extension speed is instrumental for asymmetrical targeting.....</i>	<i>22</i>
DISCUSSION	23
MATERIALS AND METHODS	31
REFERENCES.....	37
 APPENDIX A - SUPPLEMENTAL MATERIAL FOR CHAPTER 2	41

List of Figures

Figure 1-1. Schematics of Neural Superposition Wiring.....	8
Figure 1-2. Schematic of eye imaginal disk development.....	9
Figure 1-3. Schematics of lamina cartridge and tetrad synapse.....	10
Figure 2-1: Changes in R3 or R4 cell identity lead to changes in final targeting.....	26
Figure 2-2: Establishment of standardized coordinates for comparison of growth cone extension.	27
Figure 2-3: Wild-type R3s and R4s exhibit asymmetric speeds but symmetric directions of extension. ..	28
Figure 2-4: Extension speed is instrumental for asymmetrical targeting.....	29
Figure A-1: Extension phenotype of wild-type flies over time.	42
Figure A-2: Variation of the standardized coordinate system across samples.	43
Figure A-3: Variation of the standardized coordinate system across time points.	44
Figure A-4: Extension phenotype of <i>sev>Fz</i> and <i>sev>N^{ic}</i> flies over time.....	45
Figure A-5: Repulsion model for determining growth cone extension angle.....	46

List of Tables

Table 2-1: Penetrance of target alteration of $sev>Fz$ and $sev>N^{ic}$	30
Table A-1: P-values for data used to create Figure 2-3.	47
Table A-2: P-values for data used to create Figure 2-4.	48

List of Abbreviations

AEL: after egg laying

APF: After Puparium Formation

Dgo: Diego

Dsh: Dishevelled

Fmi: Flamingo

Fz: Frizzled

Fz: Frizzled

Gek: Genghis Khan

Gogo: Golden Goal

hrs APF: hours After Puparium Formation

L cell: lamina monopolar cell

L1-L5: Lamina monopolar cell subtypes 1 to 5

MF: morphogenetic furrow

N-Cad: N-Cadherin

Nic: Intracellular domain of Notch

NSP: Neural Superposition

PCP: planar cell polarity

Pk: Prickle

R cell: Photoreceptor cell

R1-6: Photoreceptor subtypes 1 to 6

R7-8: Photoreceptor subtypes 7 and 8

Sdk: Sidekick

sev: sevenless

Stbm: Strabismus

T: target position

wg: wingless

Chapter 1: Background

Main Contributing Authors:

Weiyue Ji¹, Lani F. Wu², Steven J. Altschuler²

Affiliations:

¹Biophysics Graduate Group, University of California, San Francisco, San Francisco, CA 94158, USA.

²Department of Pharmaceutical Chemistry, University of California, San Francisco, San Francisco, CA 94158, USA

Introduction

How do a limited number of protein-coding genes in our genome lead to the impressively complicated but highly ordered connectivity patterns in the brain? This is a fascinating question in neuronal development that remains a mystery. Many studies have focused on identifying various “guidance cues” that encode distinct “addresses” of targets that growing axons recognize and discovering how the molecules are spatiotemporally controlled to restrict the searching space. However, this code-matching theory is most likely not the entire story of brain wiring: such a precise and deterministic molecular code could be as complex as the wiring diagrams themselves [1]. The existence of target-independent, self-organization processes among growing axons that control their own robust wiring could be an explanation for this paradox. This self-organization principle is best exemplified in sensory circuit formation [2], where pre- and post-synaptic neurons connect with stereotypical topographical mapping. However, how the self-organization principle is executed by simple rules of individual presynaptic axons, and how this robust self-organization contributes to the final wiring precision, remain largely understudied.

The *Drosophila* visual system, where the light-sensing retina (compound eye) transmit signals to the optic lobe (four consecutive neuropil regions: lamina, medulla, lobula, and lobula plate), represents a remarkable instance to study design principles of sensory circuits: it has a complex yet robust wiring circuit, its relatively small size and short developmental period are amenable to cutting edge imaging techniques, and we have sufficient genetic tools to manipulate its developmental process with high spatiotemporal resolution.

The compound eye of the fruit fly is comprised of ~800 ommatidia (unit eyes), each containing 8 photoreceptors of distinct types (R1-R8). Photoreceptors of individual ommatidium are organized in a trapezoid shape, with R1-R6s on the periphery (“outer” photoreceptors, responsible for motion detection) and R7/8 in the inside (“inner” photoreceptors, responsible for color vision). The trapezoids are precisely aligned along the anterior-posterior and dorsal-ventral axes of the eye, with the dorsal and ventral parts mirror-symmetrizing each other (Figure 1-1A). Outer and inner photoreceptors connect to different layers in the optic lobe, both forming columnar structures: R1-R6s forms “cartridges” with lamina monopolar

cells (L cells, L1-L5) in the lamina layer, while R7-R8s forms “columns” with various neurons in the medulla layer. Outer photoreceptors connect to L cells in a complex yet stereotypical manner. Due to the shape of the compound eye and ommatidia, outer photoreceptors within each ommatidium receives light inputs from different points in space, and hence requires re-sorting in the lamina: R1-R6 from the same ommatidium diverge towards 6 different L cell regions (or target positions, T1-T6), and, at each target position, R1-R6 cells converge, each cell originating from a different ommatidium (Figure 1-1B). This remarkable axonal resorting process in the lamina is referred to as neural superposition (NSP) [3–6].

The development and wiring of R1-R6 cells have been extensively studied. The entire process can be divided into a series of temporally distinct and genetically separable steps: 1) Photoreceptors are born and specified in the eye imaginal disk and migrate out of the eye disk to form the lamina plexus. 2) Growth cones of photoreceptors resort in the lamina to find correct targets (NSP wiring). 3) Photoreceptor synapse with L cells and other cell types and form lamina cartridges. (Figure 1-1C) [4,6]. Below, I will briefly summarize the main events of each step.

Photoreceptor differentiation in the eye imaginal disk

The *Drosophila* eye imaginal disk develops in a temporal wave. A morphogenetic furrow (MF) sweeps across the developing eye disk from posterior to anterior, specifying a new row of photoreceptor clusters roughly every 2 hours [7,8]. Anterior to the furrow, R cells are recruited and specified sequentially from a pool of undifferentiated cells [9–12]. R8 is the first to be recruited, followed by pairwise recruitment of R2/R5 and R3/R4. These 5 cells form a symmetrical structure called the “five-cell precluster”. Later, the symmetry of the precluster breaks when R3/R4 precursors start to differentiate. Finally, the undifferentiated cell pool undergoes another round of division (“second mitotic wave”), from which R1/R6 and R7 are recruited. It will take around 2 days for all photoreceptor clusters to form in the eye disk. [9,13,14]

A crucial step in establishing the asymmetry of the photoreceptor preclusters, and the subsequent orientation of the adult ommatidium trapezoid, is the specification of R3/R4 fate and the rotation of the photoreceptor preclusters in accordance with the equator (Figure 1-2) [15]. During the early third instar

larval stage, *wingless* (*wg*) is expressed at both the dorsal and ventral pole of the eye disk and forms a gradient that is lowest in the middle, which defines the “equator” [16,17]. After the five-cell precluster is formed, the R3/R4 precursors start to differentiate, with the cells closer to the equator adopting the R3 fate. This process is controlled by molecules from the planar cell polarity (PCP) pathway, such as Frizzled (Fz) [18–22], Dishevelled (Dsh) [19,22–24], Strabismus (Stbm, a.k.a. Van-gogh, Vang) [25], Flamingo (Fmi) [22,26,27], Prickle (Pk, a.k.a. Prickle-spiny legs) [18,28], and Diego (Dgo) [29], with Notch-Delta pathway in the downstream of PCP molecules reinforcing the fate asymmetry [20,21,30,31]. At the same time, the five-cell preclusters from the dorsal and ventral side of the equator start to rotate 45° in opposing directions, with the dorsal side rotating clockwise and the ventral side counterclockwise [32,33]. After the recruitment of R1/R6 and R7 cells, the cluster slowly rotates another 45° until they are 90° with respect to their initial orientation near the MF, controlled by PCP downstream molecule Nemo [34].

Photoreceptor axon pathfinding to the lamina

Like the development of the eye imaginal disk, photoreceptors project their axons into the optic lobe in a similar temporal wave. Shortly after differentiation, R cell axons start migrating out of the eye imaginal disk in the same subtype-specific order as they were differentiated. These axons are divided into axonal bundles by glial cells that ensheathed them [4]. Axonal bundles terminate between two layers of glial cells [35], which in turn initiate the proliferation and differentiation of L cells (their target cells) [36], thus forming the lamina plexus. Landing sites of R cell axons from one single bundle form a horse-shoe-like structure in the lamina plexus, surrounding the dendrites of L cells [37]. Thereby, R cell axons and L cell neurites establish two distinct grids – “heel” grid from landing points of R cell axons and “target” grid from neurites of L cells – which is a prerequisite for subsequent visual map formation [37]. Mutant analysis suggests that membrane receptor Golden Goal (Gogo) [38] and cell adhesion molecule Sidekick (Sdk) [39] may be involved in the formation of regular heel and target grids.

Photoreceptor resorting in the lamina

At ~20 hrs APF, photoreceptors have finished the differentiation and axon pathfinding process, and the entire lamina plexus is formed [37]. The next step is for the growth cones of the R cells to extend laterally in the lamina plexus towards their prospective targets. While the heel and target grids are established in a temporal wave, it seems that the extension of growth cones starts synchronously across the posterior-anterior axis [37,40]. This synchronization of neuronal wiring after initial axon pathfinding appears to be a global theme in optic lobe development, as shown in recent single-cell transcriptomic studies [41,42]. It has also been shown that R cells exhibit relatively consistent and cell type-specific velocity throughout the extension process [37].

Mutant analysis has provided key insights into mechanisms of R-cell resorting. A study from Clandinin and Zipursky [43] suggested that the ommatidial orientation of the originating bundle contribute to the trajectories of growth cones. Subsequent studies have identified many molecules that are involved in the process, including Genghis Khan (Gek) [44], Flamingo (Fmi) [40,45,46], N-Cadherin (N-Cad) [40,47–49], as well as LAR [50] and Liprin- α [50,51] which interacts with N-Cad [49]. Among these molecules, cadherins Fmi and N-Cad are of particular interest. Specifically, they were reported to work together [40] in determining target specificity: Fmi was suggested to act as a homophilic receptor that mediates level-dependent, cell non-autonomous interactions between R cell growth cones to adjust their growth trajectory [46], while N-Cad was shown to have a partially redundant role with Fmi in mediating multiple growth cone interactions and thus controls R cell targeting [40].

Intra-vital imaging and mathematical modeling provided additional insight into the general principles of NSP wiring. Observations from data-driven computational modeling suggested that interaction among R cells are crucial for target recognition, and that L cells may not be necessary for the correct formation of NSP map [37]: A “quorum sensing” mechanism with only R-R interactions was quite robust to varying degrees of interaction strength, while mechanisms only containing R-L interactions were too sensitive to noise. Their modeling even recapitulated the observed increase in sorting defects near the

equator, providing strong evidence that it accurately represents some aspect of the general principles of the NSP wiring process [37].

Lamina cartridge and synapse formation

The lateral extension of R cell growth cones stop at ~36 hrs APF, when all R cells have established contact with their targets. R cell growth cones then start extending perpendicular to the lamina plexus, creating a tubular column structure – the lamina “cartridges” [4]. Meanwhile, L1 and L2 cells extend filopodia between the R cell columns and initiate the synapse formation process [4,52].

In a standard lamina cartridge, R1-R6 axons form a circle surrounding L1 and L2 neurites, while most neurites of L3, L4, and L5 are in the periphery of each cartridge [53] (Figure 1-3A). This stereotypical organization has been shown to depend on differential adhesion of N-Cad [54] and is thought to facilitate efficient synapse formation [53,54].

After mid-pupal stage (~50 hrs APF), presynaptic densities, namely “T-bars”, start to emerge on the intersection between R and L cell processes, which indicate the initiation of synapse formation [4]. When forming synapses, R and L cells are also organized characteristically (“tetrad synapses”): at each tetrad synapse, R cell makes connection with for other post-synaptic cells, two of which are always L1 and L2 cells, while the other two cells can vary (L3, amacrine (Am), or glial cells) (Figure 1-3B) [53,55]. On average, each R cell cartridge forms about 50 tetrad synapses [56,57]. This synapse formation process is both independent of accurate wiring and synaptic activity [58], making NSP wiring a genetically “hard-wired” neural circuit.

Summary

Visual map formation in the lamina of *Drosophila* is a highly robust pattern formation process [3,40,58–60]. Despite over 50 years of research, we still don’t fully understand how such a complicated resorting process is executed with astonishing accuracy. For example, how mechanistically separable are

the distinct steps of NSP wiring? Why and how do photoreceptors start extending synchronously while they arrive at the lamina plexus in a temporal fashion? How do photoreceptors determine their subtype-specific extension velocity, when most of them do not make contact with their putative target in the beginning of NSP wiring? In the next chapter, I will try to address the last question, investigating how extension velocity of photoreceptors might be controlled.

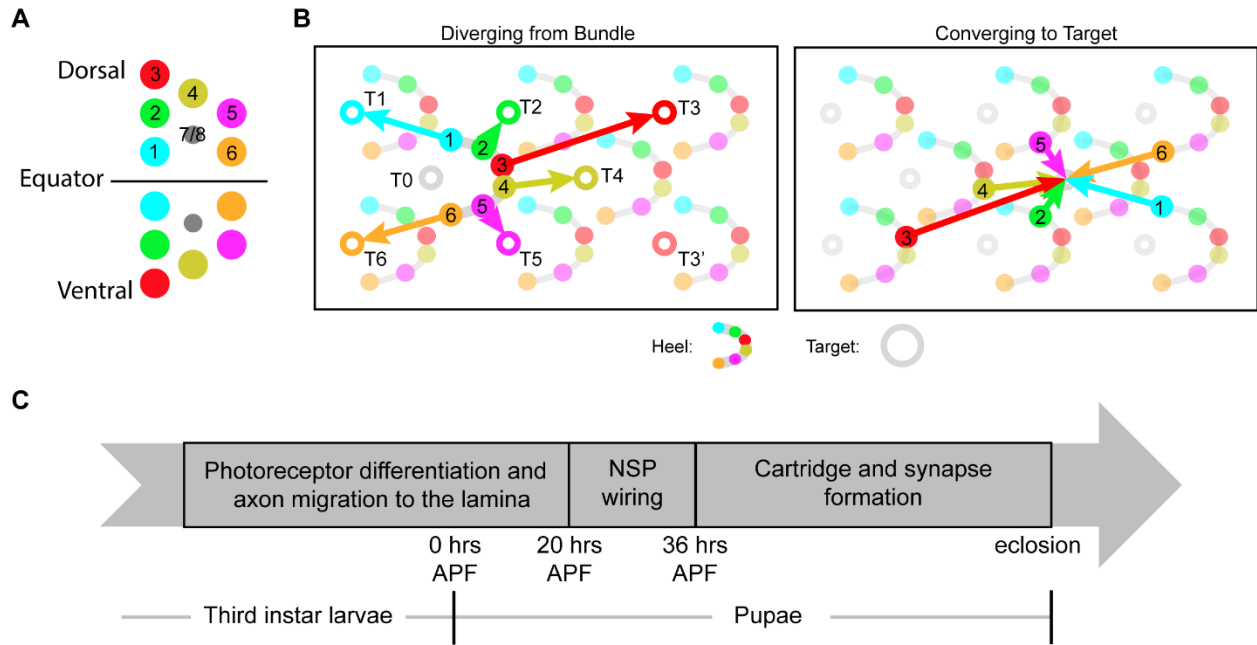


Figure 1-1. Schematics of Neural Superposition Wiring

(A) Orientation of trapezoid ommatidia in dorsal vs ventral part of the eye. (B) NSP wiring topology. Solid circles: Landing points of R1-R6 at the lamina (“heels”); open circles: target locations of R1-R6 growth cones. T3’: target of fate-altered R3s; T0: target located within the bundle of interest (though targeted by R cells from other bundles in NSP wiring). R1-R6 are color coded consistently in all schematics. (C) Timing of NSP wiring. APF: “After Puparium Formation”.

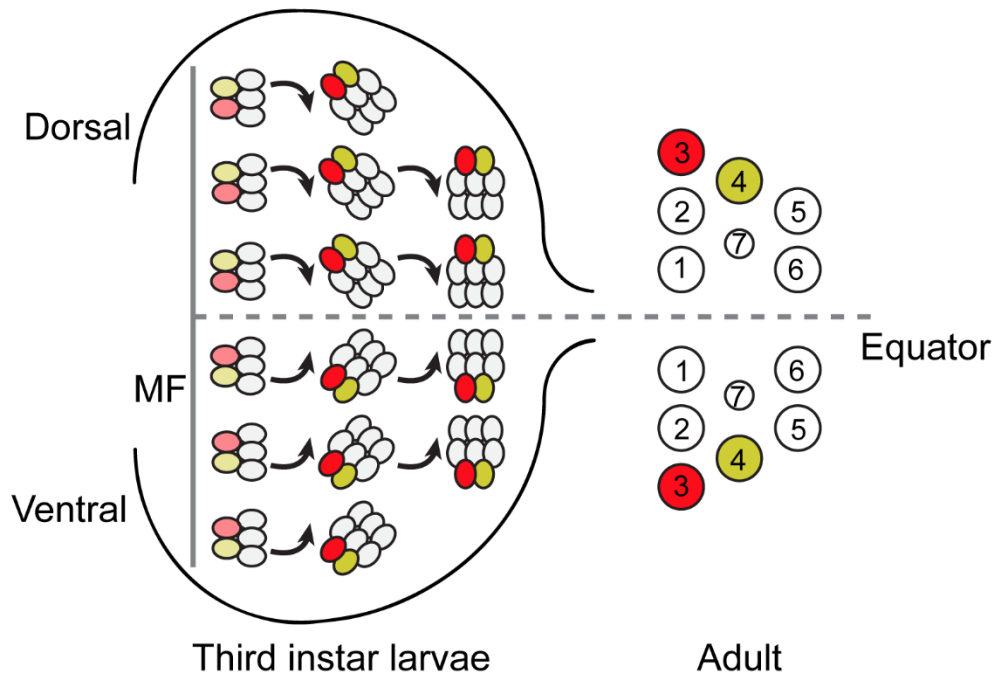


Figure 1-2. Schematic of eye imaginal disk development.

Schematic of a third instar eye imaginal disk (left) vs. adult ommatidium (right) highlighting R3/R4 pair. R3/R4 is color-coded according to Figure 1-1, while other R cells are colored white. Pale vs. opaque indicates pre vs. post specification. The solid grey line indicates the position of morphogenetic furrow (MF), while the dashed line indicates the equator. Adapted from [15].

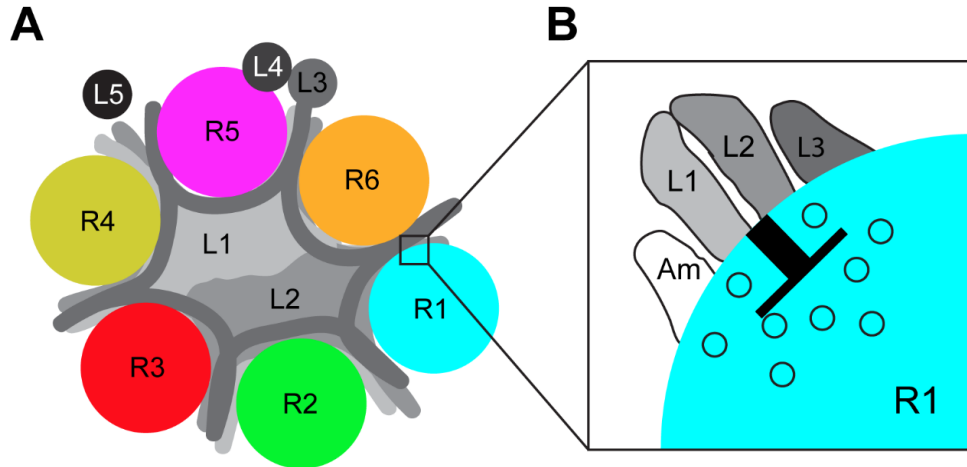


Figure 1-3. Schematics of lamina cartridge and tetrad synapse.

(A) Schematics of a cross section through a lamina cartridge. R1-R6 axons form a ring around L1-L3 dendrites. (B) Schematics of a tetrad synapse. R cells are color-coded according to Figure 1-1. L cells are colored in an increasing shade of grey. Adapted from [61].

References

1. Hassan BA, Hiesinger PR. Beyond Molecular Codes: Simple Rules to Wire Complex Brains. *Cell*. 2015;163(2):285–91.
2. Petrovic M, Schmucker D. Axonal wiring in neural development: Target-independent mechanisms help to establish precision and complexity. *Bioessays*. 2015;37(9):996–1004.
3. Horridge GA, Meinertzhagen IA. The accuracy of the patterns of connexions of the first- and second-order neurons of the visual system of *Calliphora*. *Proc Royal Soc Lond Ser B Biological Sci*. 1970;175(1038):69–82.
4. Meinertzhagen IA, Hanson TE. The development of the optic lobe. In: *The Development of Drosophila melanogaster*. Cold Spring Harbor Laboratory Press; 1993. p. 1363–491.
5. Hadjieconomou D, Timofeev K, Salecker I. A step-by-step guide to visual circuit assembly in *Drosophila*. *Curr Opin Neurobiol*. 2011;21(1):76–84.
6. Agi E, Langen M, Altschuler SJ, Wu LF, Zimmermann T, Hiesinger PR. The Evolution and Development of Neural Superposition. *J Neurogenet*. 2014;28(3–4):216–32.
7. Campos-Ortega JA, Hofbauer A. Cell clones and pattern formation: On the lineage of photoreceptor cells in the compound eye of *Drosophila*. *Wilhelm Roux's Archives Dev Biology*. 1977;181(3):227–45.
8. Tomlinson A, Ready DF. Neuronal differentiation in the *Drosophila* ommatidium. *Dev Biol*. 1987;120(2):366–76.
9. Roignant J-Y, Treisman JE. Pattern formation in the *Drosophila* eye disc. *Int J Dev Biol*. 2009;53(5–6):795–804.
10. Quan X, Ramaekers A, Hassan BA. Chapter ten Transcriptional Control of Cell Fate Specification Lessons from the Fly Retina. *Curr Top Dev Biol*. 2012;98:259–76.
11. Treisman JE. Retinal differentiation in *Drosophila*. *Wiley Interdiscip Rev Dev Biology*. 2013;2(4):545–57.
12. Nériec N, Desplan C. From the Eye to the Brain: Development of the *Drosophila* Visual System. *Curr Top Dev Biol*. 2016;116:247–71.

13. Baker NE. Patterning signals and proliferation in *Drosophila* imaginal discs. *Curr Opin Genet Dev.* 2007;17(4):287–93.
14. Tsachaki M, Sprecher SG. Genetic and developmental mechanisms underlying the formation of the *Drosophila* compound eye. *Dev Dynam.* 2012;241(1):40–56.
15. Jenny A. Current Topics in Developmental Biology. *Curr Top Dev Biol.* 2010;93:189–227.
16. Singh A, Lim J, Choi K. Dorsoventral boundary for organizing growth and planar polarity in the *Drosophila* eye. *Adv Dev Biology.* 2005;14(Semin. Cell. Dev. Biol.122001):59–90.
17. Wehrli M, Tomlinson A. Independent regulation of anterior/posterior and equatorial/polar polarity in the *Drosophila* eye; evidence for the involvement of Wnt signaling in the equatorial/polar axis. *Development.* 1998;125(8):1421–32.
18. Zheng L, Zhang J, Carthew RW. *frizzled* regulates mirror-symmetric pattern formation in the *Drosophila* eye. *Dev Camb Engl.* 1995;121(9):3045–55.
19. Strutt DI, Weber U, Mlodzik M. The role of RhoA in tissue polarity and *Frizzled* signalling. *Nature.* 1997;387(6630):292–5.
20. Tomlinson A, Struhl G. Decoding vectorial information from a gradient: sequential roles of the receptors *Frizzled* and *Notch* in establishing planar polarity in the *Drosophila* eye. *Dev Camb Engl.* 1999;126(24):5725–38.
21. Cooper MTD, Bray SJ. *Frizzled* regulation of *Notch* signalling polarizes cell fate in the *Drosophila* eye. *Nature.* 1999;397(6719):526–30.
22. Strutt D, Johnson R, Cooper K, Bray S. Asymmetric Localization of *Frizzled* and the Determination of *Notch*-Dependent Cell Fate in the *Drosophila* Eye. *Curr Biol.* 2002;12(10):813–24.
23. Theisen H, Purcell J, Bennett M, Kansagara D, Syed A, Marsh JL. *dishevelled* is required during *wingless* signaling to establish both cell polarity and cell identity. *Dev Camb Engl.* 1994;120(2):347–60.
24. Boutros M, Paricio N, Strutt DI, Mlodzik M. *Dishevelled* Activates *JNK* and Discriminates between *JNK* Pathways in Planar Polarity and *wingless* Signaling. *Cell.* 1998;94(1):109–18.

25. Wolff T, Rubin GM. Strabismus, a novel gene that regulates tissue polarity and cell fate decisions in *Drosophila*. *Dev Camb Engl*. 1998;125(6):1149–59.
26. Yang C, Axelrod JD, Simon MA. Regulation of Frizzled by Fat-like Cadherins during Planar Polarity Signaling in the *Drosophila* Compound Eye. *Cell*. 2002;108(5):675–88.
27. Das G, Reynolds-Kenneally J, Mlodzik M. The Atypical Cadherin Flamingo Links Frizzled and Notch Signaling in Planar Polarity Establishment in the *Drosophila* Eye. *Dev Cell*. 2002;2(5):655–66.
28. Gubb D, Green C, Huen D, Coulson D, Johnson G, Tree D, et al. The balance between isoforms of the Prickle LIM domain protein is critical for planar polarity in *Drosophila* imaginal discs. *Gene Dev*. 1999;13(17):2315–27.
29. Feiguin F, Hannus M, Mlodzik M, Eaton S. The Ankyrin Repeat Protein Diego Mediates Frizzled-Dependent Planar Polarization. *Dev Cell*. 2001;1(1):93–101.
30. Fortini ME, Rebay I, Caron LA, Artavanis-Tsakonas S. An activated Notch receptor blocks cell-fate commitment in the developing *Drosophila* eye. *Nature*. 1993;365(6446):555–7.
31. Fanto M, Mlodzik M. Asymmetric Notch activation specifies photoreceptors R3 and R4 and planar polarity in the *Drosophila* eye. *Nature*. 1999;397(6719):523–6.
32. Tomlinson A, Ready DF. Cell fate in the *Drosophila* ommatidium. *Dev Biol*. 1987;123(1):264–75.
33. Wolff T, Ready DF. The beginning of pattern formation in the *Drosophila* compound eye: the morphogenetic furrow and the second mitotic wave. *Development*. 1991;113(3):841–50.
34. Choi K-W, Benzer S. Rotation of photoreceptor clusters in the developing *drosophila* eye requires the *nemo* gene. *Cell*. 1994;78(1):125–36.
35. Poeck B, Fischer S, Gunning D, Zipursky SL, Salecker I. Glial Cells Mediate Target Layer Selection of Retinal Axons in the Developing Visual System of *Drosophila*. *Neuron*. 2001;29(1):99–113.
36. Huang Z, Kunes S. Hedgehog, Transmitted along Retinal Axons, Triggers Neurogenesis in the Developing Visual Centers of the *Drosophila* Brain. *Cell*. 1996;86(3):411–22.
37. Langen M, Agi E, Altschuler DJ, Wu LF, Altschuler SJ, Hiesinger PR. The Developmental Rules of Neural Superposition in *Drosophila*. *Cell*. 2015;162(1):120–33.

38. Hein I, Suzuki T, Kadow ICG. Gogo Receptor Contributes to Retinotopic Map Formation and Prevents R1-6 Photoreceptor Axon Bundling. *Plos One*. 2013;8(6):e66868.
39. Astigarraga S, Douthit J, Tarnogorska D, Creamer MS, Mano O, Clark DA, et al. *Drosophila* Sidekick is required in developing photoreceptors to enable visual motion detection. *Development*. 2018;145(3):dev158246.
40. Schwabe T, Neuert H, Clandinin TR. A Network of Cadherin-Mediated Interactions Polarizes Growth Cones to Determine Targeting Specificity. *Cell*. 2013;154(2):351–64.
41. Özel MN, Simon F, Jafari S, Holguera I, Chen Y-C, Benhra N, et al. Neuronal diversity and convergence in a visual system developmental atlas. *Nature*. 2021;589(7840):88–95.
42. Kurmangaliyev YZ, Yoo J, Valdes-Aleman J, Sanfilippo P, Zipursky SL. Transcriptional Programs of Circuit Assembly in the *Drosophila* Visual System. *Neuron*. 2020;108(6):1045-1057.e6.
43. Clandinin TR, Zipursky SL. Afferent Growth Cone Interactions Control Synaptic Specificity in the *Drosophila* Visual System. *Neuron*. 2000;28(2):427–36.
44. Gontang AC, Hwa JJ, Mast JD, Schwabe T, Clandinin TR. The cytoskeletal regulator Genghis khan is required for columnar target specificity in the *Drosophila* visual system. *Development*. 2011;138(22):4899–909.
45. Lee RC, Clandinin TR, Lee C-H, Chen P-L, Meinertzhagen IA, Zipursky SL. The protocadherin Flamingo is required for axon target selection in the *Drosophila* visual system. *Nat Neurosci*. 2003;6(6):557–63.
46. Chen P-L, Clandinin TR. The Cadherin Flamingo Mediates Level-Dependent Interactions that Guide Photoreceptor Target Choice in *Drosophila*. *Neuron*. 2008;58(1):26–33.
47. Lee C-H, Herman T, Clandinin TR, Lee R, Zipursky SL. N-Cadherin Regulates Target Specificity in the *Drosophila* Visual System. *Neuron*. 2001;30(2):437–50.
48. Prakash S, Caldwell JC, Eberl DF, Clandinin TR. *Drosophila* N-cadherin mediates an attractive interaction between photoreceptor axons and their targets. *Nat Neurosci*. 2005;8(4):443–50.

49. Prakash S, McLendon HM, Dubreuil CI, Ghose A, Hwa J, Dennehy KA, et al. Complex interactions amongst N-cadherin, DLAR, and Liprin- α regulate *Drosophila* photoreceptor axon targeting. *Dev Biol.* 2009;336(1):10–9.
50. Clandinin TR, Lee C-H, Herman T, Lee RC, Yang AY, Ovasapyan S, et al. *Drosophila* LAR Regulates R1-R6 and R7 Target Specificity in the Visual System. *Neuron.* 2001;32(2):237–48.
51. Choe K-M, Prakash S, Bright A, Clandinin TR. Liprin- is required for photoreceptor target selection in *Drosophila*. *Proc National Acad Sci.* 2006;103(31):11601–6.
52. Meinertzhagen IA, Piper ST, Sun X -J., Fröhlich A. Neurite morphogenesis of identified visual interneurons and its relationship to photoreceptor synaptogenesis in the flies, *Musca domestica* and *Drosophila melanogaster*. *Eur J Neurosci.* 2000;12(4):1342–56.
53. Rivera-Alba M, Vitaladevuni SN, Mishchenko Y, Lu Z, Takemura S, Scheffer L, et al. Wiring Economy and Volume Exclusion Determine Neuronal Placement in the *Drosophila* Brain. *Curr Biol.* 2011;21(23):2000–5.
54. Schwabe T, Borycz JA, Meinertzhagen IA, Clandinin TR. Differential Adhesion Determines the Organization of Synaptic Fascicles in the *Drosophila* Visual System. *Curr Biol.* 2014;24(12):1304–13.
55. Meinertzhagen IA, O’Neil SD. Synaptic organization of columnar elements in the lamina of the wild type in *Drosophila melanogaster*. *J Comp Neurol.* 1991;305(2):232–63.
56. Meinertzhagen IA, Hu X. Evidence for site selection during synaptogenesis: the surface distribution of synaptic sites in photoreceptor terminals of the flies *Musca* and *Drosophila*. *Cellular and Molecular Neurobiology* [Internet]. 1996 Dec 1;16(6):pages677-698. Available from: <https://link.springer.com/article/10.1007%2F02151904>
57. Meinertzhagen IA, Sorra KE. Chapter 3 Synaptic organization in the fly’s optic lamina: few cells, many synapses and divergent microcircuits. *Prog Brain Res.* 2001;131:53–69.
58. Hiesinger PR, Zhai RG, Zhou Y, Koh T-W, Mehta SQ, Schulze KL, et al. Activity-Independent Predispecification of Synaptic Partners in the Visual Map of *Drosophila*. *Curr Biol.* 2006;16(18):1835–43.

59. Braitenberg V. Patterns of projection in the visual system of the fly. I. Retina-lamina projections. *Exp Brain Res.* 1967;3(3):271–98.
60. Meinertzhagen IA. Erroneous projection of retinula axons beneath a dislocation in the retinal equator of *Calliphora*. *Brain Res.* 1972;41(1):39–49.
61. Millard SS, Pecot MY. Strategies for assembling columns and layers in the *Drosophila* visual system. *Neural Dev.* 2018;13(1):11.

Chapter 2: Analysis of growth cone extension in standardized coordinates highlights self-organization rules during wiring of the *Drosophila* visual system

Main Contributing Authors:

Weiyue Ji¹, Lani F. Wu², Steven J. Altschuler²

Affiliations:

¹Biophysics Graduate Group, University of California, San Francisco, San Francisco, CA 94158, USA.

²Department of Pharmaceutical Chemistry, University of California, San Francisco, San Francisco, CA 94158, USA

Abstract

A fascinating question in neuroscience is how ensembles of neurons, originating from different locations, extend to the proper place and by the right time to create precise circuits. Here, we investigate this question in the *Drosophila* visual system, where photoreceptors re-sort in the lamina to form the crystalline-like neural superposition circuit. The repeated nature of this circuit allowed us to establish a data-driven, standardized coordinate system for quantitative comparison of growth cones within and across samples. Using this common frame of reference, we investigated the extension of the R3 and R4 photoreceptors, which is the only pair of symmetrically arranged photoreceptors with asymmetric target choices. We found that extension speeds of the R3 and R4 growth cones are inherent to their cell identities, while extension angles are better predicted by a weighted nearest-neighbor repulsion model. The ability to parameterize local regularity in tissue organization facilitated the characterization of ensemble cellular behaviors and dissection of mechanisms governing neural circuit formation.

Introduction

Convergence of neurons at the same time and place can be crucial for subsequent interactions, such as synaptic competition [1–3]. Yet ways in which this is achieved, beyond the presence of guidance cues, is less well understood. The *Drosophila* visual system, especially the process of neural superposition (NSP) wiring, offers a remarkable opportunity to identify cell autonomous and non-autonomous principles underlying how such kinetic patterning can occur.

As reviewed in chapter 1, this system has been extensively studied. An intriguing discovery from one previous study [4] is that R1-R6 each exhibit relatively consistent and cell type-specific velocity during growth cone extension. This suggests that the velocity of growth cones plays a pivotal role in their synaptic partner selection. Previous studies suggested that both ommatidia orientation of the originating bundle [5] and interactions among growth cones within the same and neighboring bundles [6,7] contribute to the direction of R cell projections. However, how extension velocity of photoreceptor growth cones is controlled remains unclear.

To address this question, we developed a data-driven standardized coordinate system around each bundle built upon the lattice-like structure of the NSP circuit. This enabled the characterization of ensemble behaviors of photoreceptor cell types, despite morphological variability and stochastic differences of individual neurons and local warping of the lattice. We then used these coordinates to investigate the influence of cell identity and nearest neighbors on R3 and R4 growth cone speed and direction. These quantitative studies helped assess the degree to which cell autonomous and non-autonomous mechanisms control the speed and direction of growth cone extension during NSP circuit formation.

Results

Changes in R3 or R4 cell identity lead to changes in final targeting

The early role of photoreceptor identity during eye development is well documented. R1-R6s develop in three sequential pairs during eye development: R2/R5, then R3/R4 and last R1/R6. The R3/R4

pair is particularly important in breaking the symmetry of the R-cell cluster, including the 90-degree rotation of R-cell clusters in the developing eye disc and the asymmetric trapezoidal arrangement of the adult ommatidia (See Chapter 1 for a detailed review). Interestingly, the R3/R4 pair also breaks symmetry of the NSP wiring diagram. The target positions of R3 and R4 (“T3” and “T4”, respectively) are asymmetrical, while the target positions of the other two pairs (R1/R6, R2/R5) are symmetrical (Figure 1-1B). Thus, we focused our effort on understanding the role of R3/R4 identities—and their contribution to asymmetric targeting—during the NSP wiring process in the lamina.

To alter R3 and R4 cell identities, we used genetic perturbations in the planar-cell-polarity pathway. Specifically, over-expression of Frizzled (*Fz*) with *sevenless* (*sev*) enhancer (*sev>Fz*) generates ommatidia with two R3s [8,9], while over-expression of the intracellular domain of Notch (*N^{ic}*) under the same enhancer (*sev>N^{ic}*) generates ommatidia with two R4s [10,11]. To visualize the perturbed bundles, we used a membrane-bound red fluorescent protein (tdTomato) under the same enhancer. Since the lamina plexus is densely packed with photoreceptors, it is challenging to disambiguate individual photoreceptor growth cones. Thus, we induced our perturbation sparsely. We utilized an FRT-dependent GAL80 “flip-in” construct together with a heat-shock activated flippase to generate sparse clones of perturbed bundles [12,13]. Further, to differentiate between R3 and R4 cell types at an early stage of development in both the ommatidia and lamina, we utilized the R4-specific enhancer *mδ05* fused with a membrane GFP protein (*mδ-GFP*) [10].

We visually inspected specimens of sparsely perturbed *sev>Fz* and *sev>N^{ic}* flies after the completion of NSP wiring (> 36 hours after puparium formation, or hrs APF; see Figure 1-1C for timeline [14]). We found that changes in cell identity resulted in changes in final targeting (Figure 2-1). For bundles with two R4 photoreceptors, both the normal and fate-transformed R4s target the same canonical R4 target, T4. For bundles with two R3 photoreceptors, the normal R3 targets the canonical R3 target, T3, while the fate-transformed R3 targets T3', a new target position that is mirror-symmetric to T3, instead of the original T3. (See Table 2-1 for phenotype penetrance.) This result raised the hypothesis that cell identity and the position of cells within the bundle could influence the targeting of R3 and R4 photoreceptors.

Wild-type R3s and R4s exhibit asymmetric speeds but symmetric directions of extension

Perturbing R3 and R4 cell identity changed the final target choice. We next investigated the role of cell identity during early extension. We visually examined changes in the morphologies of R3 and R4 growth cones from early to late stage of NSP (captured every 2 hrs from 22 hrs APF to 36 hrs APF). During this time, growth cones of both R3s and R4s had one (or a small number of) long filopodia extending in the same direction as the polarized leading edge (Figure A-1). The R-cell type growth cone morphologies of fixed-tissue time series appeared visually similar across samples and were consistent with published live-imaging data [4].

Searching for general rules governing wiring requires observing and analyzing large numbers of clearly distinguishable neurons, which can be impractical using intravital imaging. To overcome this limitation, we chose to quantify sparsely labeled, fixed-tissue samples, which provided relatively large numbers of growth cones across developmental time points. However, this required development of new analytical tools, as comparative analysis of growth cones within and across tissue samples is confounded by variations in image orientation, local warping of the lamina plexus, and inherent cell-cell variability. We developed a “standardized” coordinate system that utilizes the regularity of NSP circuit to align local bundle configurations (Figure 2-2; Methods). In neural superposition, there are two distinct grid-like structures: one “heel grid,” formed by the landing positions of the photoreceptors in the lamina, and one “target grid,” formed by the dendrites of their targets, the lamina monopolar cells (Figure 1-1B). The alignment of these two grids provides the local regularity needed to define the standardized coordinates.

For each bundle, we identified the starting positions of all R-cells (Heel grid, Figure 2-2A) and their putative targets (Target grid, Figure 2-2B). We also identified a center point “C”, which lies at the intersection of the line connecting R3 and T3 and the line connecting R4 and T3'. We then extrapolated polar coordinates by normalizing (Figure 2-2C): 1) length, so that $|C-T4| = 1$ ($7.2 \pm 1.5 \mu\text{m}$ before normalization); and 2) angle, so that $\angle(T3,C,T4) = \angle(T4,C,T3') = 1$ ($\angle(T3,C,T4) = 13.2^\circ \pm 3.7^\circ$, $\angle(T4,C,T3') = 14.9^\circ \pm 4^\circ$ before normalization), and that T3 and T3' were placed at angles +1 and -1, respectively. The standardized coordinates, defined by the center points and normalization for each local

region, allowed us to register bundles within and across samples (Figures A-2 and A-3) and identify ensemble behaviors of R3 and R4 cell types. This approach is designed to characterize relative, rather than absolute, changes in length or angle of extending growth cones with respect to the normalized and invariant target grid.

For each R3 or R4 growth cone, we estimated its angle and speed towards their putative targets. We chose to define the “front” of the growth cone by the average fluorescence intensity at the leading edge (Methods); this measurement of leading-edge filopodia provided a fiducial for approximating growth cone extension. Based on ensemble measurements, R3 and R4 arrive at their target regions by 28 hrs APF (Figure 2-3A). However, R3 has to travel considerably further and therefore must have higher extension speed (in agreement with previous findings [4]). Further, R3 and R4 initially have symmetric extension angles until they reach their targets at 28 hrs APF (this symmetry breaks after 28 hrs APF when the leading edges adhere to their asymmetrically positioned targets; Figure 2-3B).

Extension speed is instrumental for asymmetrical targeting

Based on these observations in wild-type, we hypothesized that extension speed plays a key role in the asymmetrical targeting of R3/R4 pairs. To test this hypothesis, we examined the behavior of sparsely perturbed mutant (*sev>Fz* and *sev>N^{tc}*) fly specimens that have both wild-type-like and fate-transformed bundles at 24 or 28 hrs APF, corresponding to early or late stages of their extension (Figures 2-4 and A-4).

We compared the ensemble behaviors of fate-transformed to wild-type bundles. The fate-transformed bundles contain either two R3s or two R4s (one of which is fate transformed and the other wild-type). We observed that the extension speed and angle of the wild-type cells in the fate-transformed bundles is similar to the R cells of the same fate in the wild-type-like bundles. More importantly, we discovered that within the fate-transformed bundles, the two R3's or two R4's extend at similar speeds and symmetric angles (Figure 2-4). Thus, we concluded that cell fate is instrumental in determining extension speed of photoreceptor growth cones, and the asymmetrical speeds of R3 vs R4 ultimately result in their asymmetrical targeting.

Taken together, the initial directions of extension for R-cells at the R3 and R4 positions are mirror symmetric and independent of cell fate (i.e., whether wild-type or fate-transformed). What could determine the initial extension directions? Previous work [6,7] suggested that interactions among neighboring growth cones may be responsible for extension direction determination. Further, re-examination of the geometric configurations of R-cell bundles and their targeting positions [4] suggested the appealing possibility of a simple repulsion rule—equal repulsion from immediate neighbor(s) within the same bundle determine the extension direction of an R cell. While this appeared reasonable for most of the R cells, R3/4 have asymmetrical targets and it was unclear how this rule could apply to their initial extension directions. In light of the discovery that R3 and R4 initially extend symmetrically, we made use of our standardized coordinate system to computationally evaluate whether a simple repulsion rule agrees with the experimental data (Figure A-5A). Analysis showed that equal repulsion would lead to predicted extension angles that are $\sim 30^\circ$ further from the bundle midline than those that are experimentally measured (Figure A-5B). Instead, regression analysis suggested that R2 or R5 contribute $\sim 2x$ the repulsion of the other immediate neighbor R3 or R4 (e.g., for the case of R3, R2 has twice the repulsion of R4) (Figure A-5B). Thus, our analysis suggests the hypothesis that unequal repulsion from R3/R4 neighbors within the bundle better models their extension directions during early patterning of the NSP circuit.

Discussion

Individual cells within developing tissues need to make decisions about their movement velocities in order to arrive at a final collective pattern [15,16]. A fascinating instance of collective cell migration is the patterning of neuronal circuits. How is velocity—defined by both the direction and speed of extending growth cones—controlled during neuronal development to achieve proper circuit formation? Here, we investigate this question in the context of NSP circuit, in which ~ 4800 neurons (= 800 bundles x 6 R-cell types) swap relative positions and identify their targets with astonishing accuracy [7,17–20].

To compare growth cone velocity across populations of neurons, we developed a standardized coordinate system for describing growth cone morphology. This coordinate system was essential in overcoming bundle-to-bundle and fly-to-fly heterogeneity, and similar approaches could be adapted to quantify and compare the dynamics of neurons in other developmental systems with other wiring geometries. We found that cell identities for R3 and R4 neurons determine their speed but not direction of extension. As a consequence, while R3 and R4 start with symmetric extension directions, their differences in speed lead to extension length differences by the final time of wiring and subsequently to asymmetric target choices. These observations highlight a crucial role for cell-autonomous mechanisms in controlling the dynamics of neuronal extension and, ultimately, the spatial-temporal coincidence of presynaptic and postsynaptic neurons.

A potential self-organizing mechanism to determine extension direction of photoreceptor growth cones is through repulsion of neighboring growth cones within the same bundle. We discovered that a simple repulsion model—where each R cell contributes equally—is not sufficient to explain the measured extension direction; rather, a model is supported in which R2/5 contributes much more strongly than R3/4. Such differential repulsion could arise through different strengths of expressed repulsive cues among neighboring cells. Interestingly, previous studies did show that Flamingo, a seven-pass transmembrane cadherin capable of inducing repulsion in both axons and dendrites [21,22], is differentially expressed amongst the different R-cell types, with R2/R5 having ~3x the expression levels of R3/R4 [7]. Our study provides a testable prediction and quantitative framework for future studies of how initial extension directions are determined, for example by examining mutants that alter the bundle configuration.

Our study also provided a functional readout and framework for future investigations into mechanisms of how cell identity controls growth cone dynamics. Regulation of cytoskeletal dynamics is a clear possibility. Studies in cultured mammalian neurons have identified key components of the cytoskeleton that regulate axon outgrowth and how these components can be regulated by signaling molecules [23,24]. For example, the cell-surface receptor Notch has been shown to regulate the speed of neurite outgrowth [25–27] via controlling the stability of microtubules [28] and the expression levels of

signaling proteins [29]. Since Notch is both key in R3/R4 fate determination and has the potential to influence extension speed, these two properties may be intertwined, and further investigation is needed to fully understand the role of Notch in NSP wiring. Additionally, while we focused on extension velocity, our findings do not exclude other factors that may also contribute to growth cone wiring that are also changed when cell identity is transformed. Understanding how cell identities translate to differences in molecular profiles and finally to changes in the cytoskeletal networks that control growth cone morphology and filopodial dynamics [30], will provide valuable insight into how extension velocity can be controlled during neuronal circuit development *in vivo*.

Coordinated arrival of neurons is thought to be crucial in ensuring point-to-point connectivity of multiple mammalian complex circuits, including the neuromuscular map [31], ocular dominance columns [32], and Purkinje cell wiring in the cerebellum [33,34]. Further, changes in the kinetics of developing neurons have been observed in multiple contexts, such as midline crossing of retinal axons [35,36] and commissural neurons [37], and the migration of Mauthner cells crossing successive motor neurons [38]. Our findings in the *Drosophila* neural superposition circuit provide a case study that connects neuronal kinetics with circuit formation, highlighting the importance of velocity control in ensuring the proper convergence of presynaptic neurons, and subsequently, the precise formation of a complex neuronal circuit.

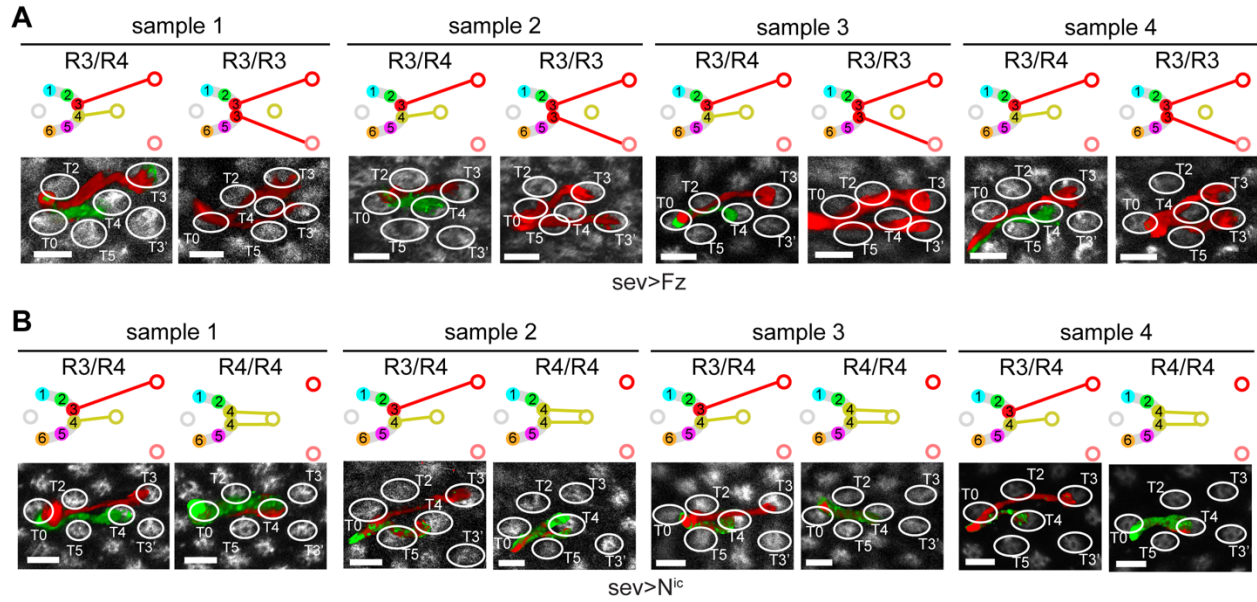


Figure 2-1: Changes in R3 or R4 cell identity lead to changes in final targeting.

Schematics (top panels) and confocal images (bottom panels) of bundles from four **(A)** *sev>Fz* (38 hrs APF) and **(B)** *sev>N^{ic}* (45 hrs APF) flies. **Top panels:** schematic of wild-type or altered wiring topology. Solid or open circles: starting points ('heels') or targets (respectively); colors coordinated between R cells and targets. T3': target of fate-altered R3s; T0: target located within the bundle of interest (though targeted by R cells from other bundles in NSP wiring). **Bottom panels:** confocal images of representative bundles. Photoreceptor growth cones are segmented and pseudo-colored (Methods) and intensity scaled for visualization. Red: *sev>RFP* expression; green: *mδ-GFP* expression; white: Fasciclin 2 (FasII) antibody staining. White ellipses: targets. Scale bar: 5 μm.

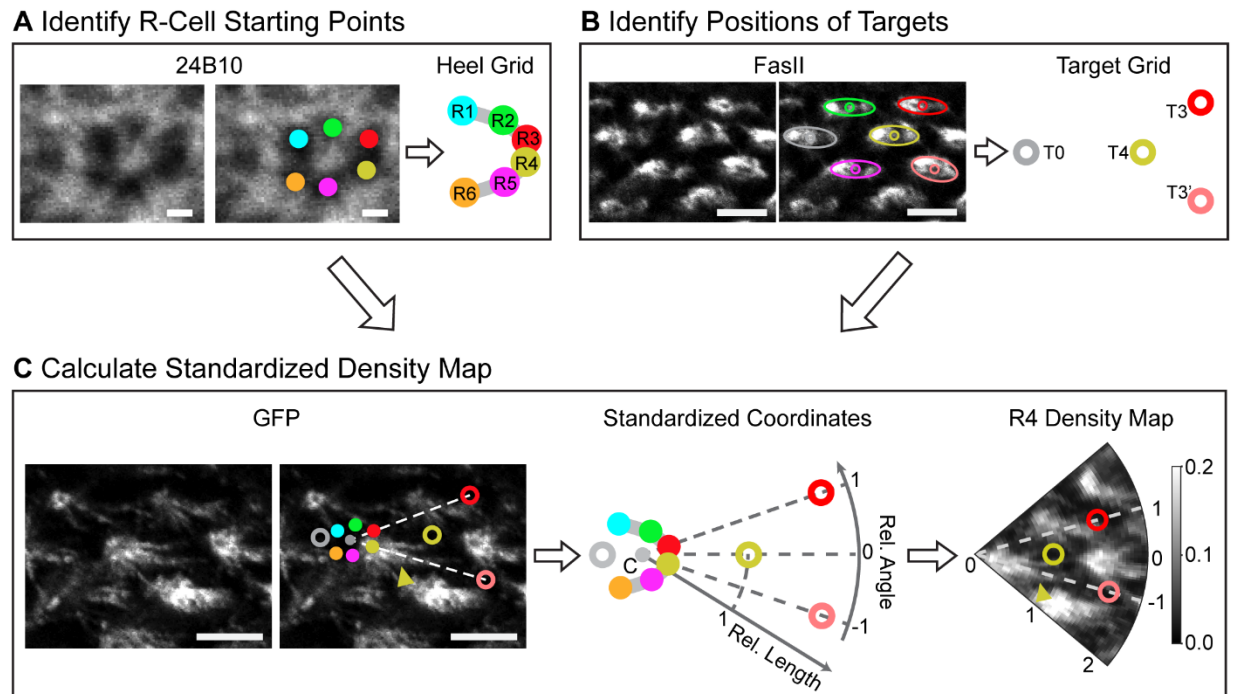


Figure 2-2: Establishment of standardized coordinates for comparison of growth cone extension.

Overview of the image quantification process. **(A)** The heel grids (i.e., R-cell extension starting points) are identified (via 24B10 antibody labeling R-cell membranes; Methods). **(B)** The target grid is identified (via FasII antibody labeling L-cell membranes; Methods). **(C)** In each region, (left) the annotation (from A-B) is used (middle) to produce standardized coordinates that are used (right) to transform confocal images into standardized density maps. This transformation allows relative lengths (radial coordinate) and angles (angular coordinate) of extending growth cones to be compared across regions. Images: confocal images of a bundle region were sampled from one wild-type fly at 26 hrs APF. Images were cropped, re-oriented and intensity scaled for visualization (Methods). Arrowheads highlights growth cone of interest. Scale bars: 5 μm for FasII and GFP images; 1 μm for 24B10 image.

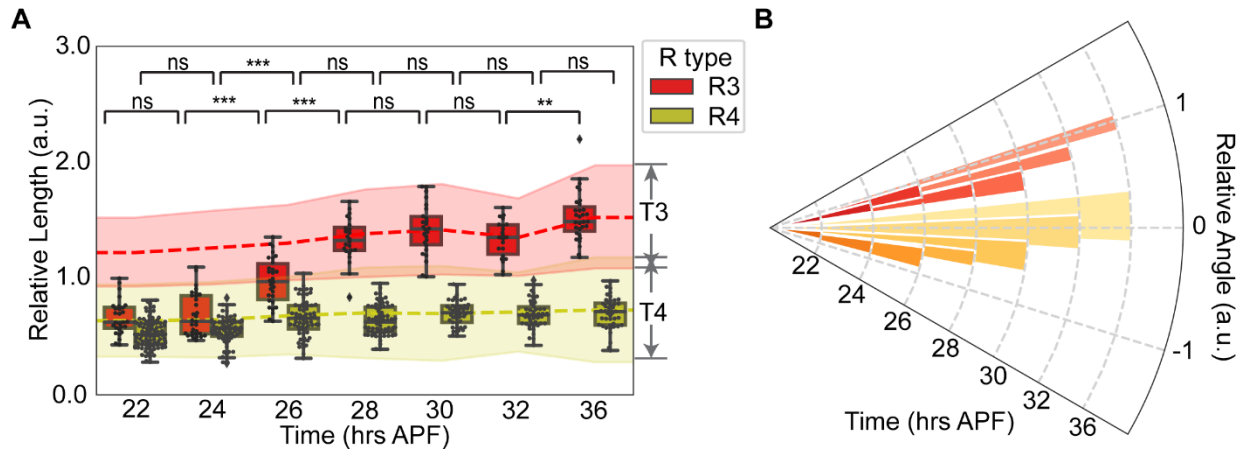


Figure 2-3: Wild-type R3s and R4s exhibit asymmetric speeds but symmetric directions of extension. **(A)** Change in relative lengths of wild-type R3 and R4 growth cones over time. Red and yellow dashed lines: mean of target centers for T3 and T4, respectively. Error bars of the dashed lines: mean of the upper and lower boundaries of targets. Significance: calculated using a two-sided Mann-Whitney test with p values adjusted by Bonferroni method. ns: $p > 0.05$, *: $0.01 < p < 0.05$, **: $0.001 < p < 0.01$, ***: $p < 0.001$. Sample sizes (number of bundles) of each time point: R3 growth cones ($n = 28, 31, 30, 24, 26, 22, 31$); R4 growth cones ($n = 96, 67, 67, 67, 44, 46, 43$). $n \geq 2$ biological replicates for each time point. See Table A-1 for p-values. **(B)** Change in relative angles of wild-type R3 and R4 growth cones over time. Red and yellow bars represent R3s and R4s, respectively. Plotted bars: radial coordinate indicates time; angle coordinate indicates mean relative angle of R3 or R4 growth cones at the given time point; and width indicates standard deviation of angle values at the given time point. Sample sizes as in (A). See Table A-1 for p-values.

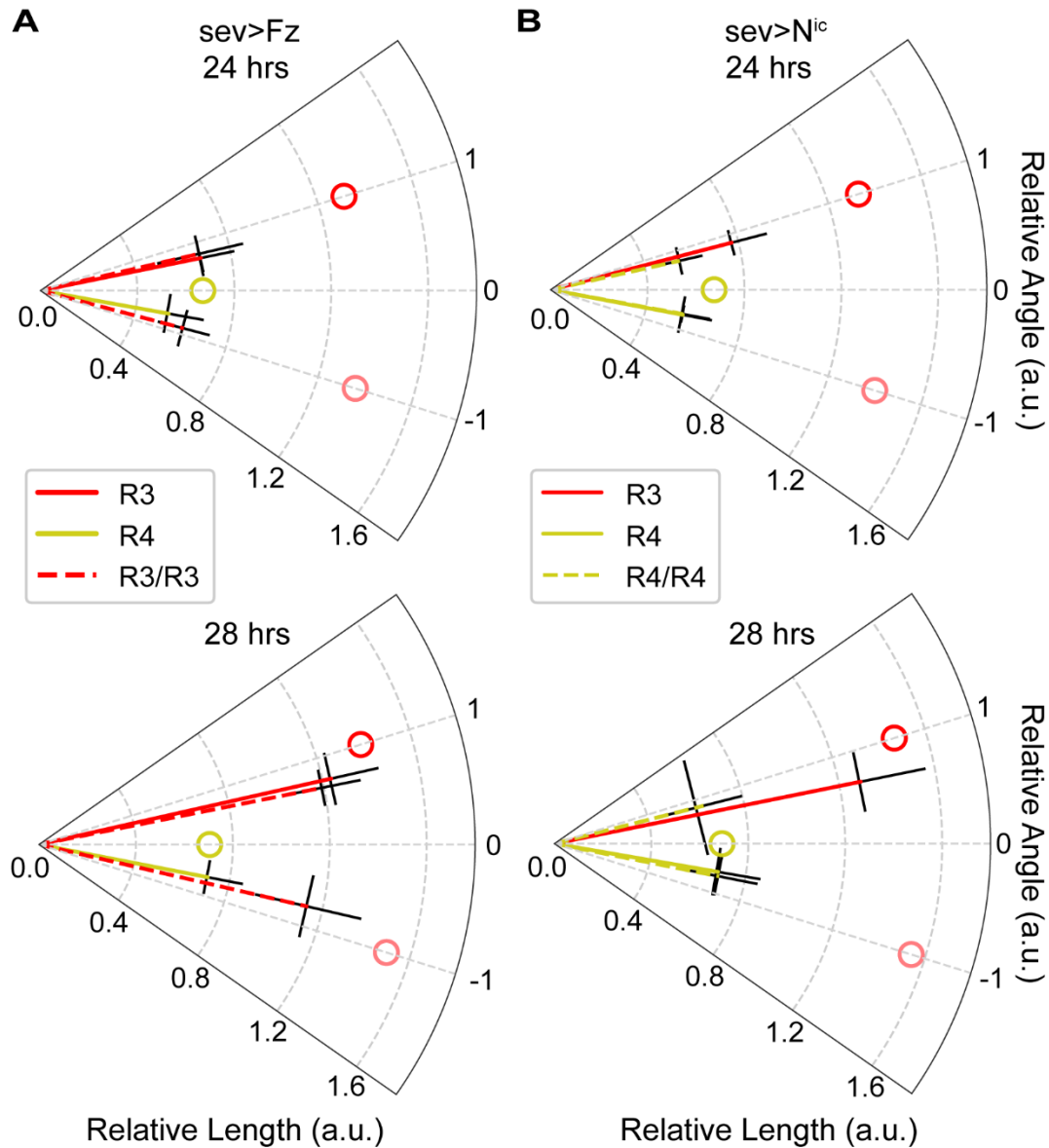


Figure 2-4: Extension speed is instrumental for asymmetrical targeting.

Polar plots of relative lengths and angles for wild-type-like (R3/R4) and perturbed (R3/R3 or R4/R4) bundles under (A) *sev>Fz* and (B) *sev>N^{ic}* conditions at 24 and 28 hrs APF. See Figure A-4 for representative images of each condition. Radial coordinate: relative length; angle coordinate: relative angle; error bars: standard deviations for length or angle. Solid lines: control bundles; dashed lines: perturbed bundles. Open circles: mean of target centers. Sample numbers for growth cones at wild-type R3 position, wild-type R4 position, perturbed R3 position, and perturbed R4 position, respectively: *sev>Fz* at 24 hrs (n = 24, 38, 10, 10) or 28 hrs (n = 52, 151, 23, 23); *sev>N^{ic}* at 24 hrs (n = 23, 46, 10, 10) or 28 hrs (n = 39, 113, 29, 29). n \geq 3 biological replicates for each genetics and time point. See Table A-2 for p-values.

Table 2-1: Penetrance of target alteration of *sev>Fz* and *sev>N^{ic}*

Images of *sev>Fz* samples at 38 hrs APF and *sev>N^{ic}* samples at 45 hrs APF were visually inspected and counted. Only bundles with two R3s (bundles with two RFP-positive R cell growth cones and no GFP-positive R cell growth cones) or bundles with two R4s (bundles with two GFP-positive R cell growth cones) are included in the counting. n = 13 biological replicates for *sev>Fz* flies and n = 5 biological replicates for *sev>N^{ic}* flies. We note that the targeting penetrance we observe is on par with that of previous studies in both this system [6,7] and others [39,40].

Genetics	Age (hrs APF)	Number of bundles with altered targeting	Number of bundles with wild-type-like targeting	Total number of bundles	Penetrance (%)
<i>sev>Fz</i>	38	15	21	36	41.7
<i>sev>N^{ic}</i>	45	48	1	49	98.0

Materials and methods

Fly stocks and handling

Fly stocks were constructed and maintained at 25 °C using standard protocols.

The following fly lines were used in this study: *tubP>stop>GAL80* (II), *tubP>stop>GAL80* (III) and *hs-FLP122* (X) (gifts from T. Clandinin, Stanford University), *mδ05-CD4::GFP* (III) (gift from P.R. Hiesinger, Free University Berlin), *Uas-N^{ic}* (II) (gift from B.A. Hassan, ICM Institute for Brain and Spinal Cord); *UAS-CD4::tdTomato* (II) (gift from L.Y. Jan and Y.N. Jan, UCSF), *UAS-fz1-1* (Bloomington Drosophila Stock Center # 41791) and *sevEP-GAL4.B* (II) (Bloomington Drosophila Stock Center # 5793).

For experiments with pupae samples, pupae with the correct genotype were collected at 0 hrs after puparium formation (APF) and aged at 28 °C to increase the penetration of genetic perturbations (Das et al., 2002). For experiments with adult samples, flies 3-5 days after eclosion were collected. Both male and female were used for all experiments.

Heat shock clone induction

Larvae with the correct genotype were heat shocked for 8 - 15 mins at 37 °C at 2 to 4 days after egg laying (AEL).

Immunohistochemistry and Imaging of Pupa Brains

Dissection and Staining

For preparation of pupal brain samples, pupal brains were dissected at the appropriate developmental stages in PBS (Phosphate Buffered Saline) and fixed with 3.7% formaldehyde-PBS for 30 mins. Fixed brains were washed three times in PBT (PBS with 0.4% Triton X-100) at room temperature and then blocked with PBT-BSA (3% Bovine Serum Albumin in PBT) for 1 hour. Two rounds of antibody staining were then performed. In each round, brains were incubated with cocktails of primary antibodies at 4°C overnight, rinsed in PBT, then incubated with cocktails of secondary antibodies at 4°C overnight or for 2 hrs at room temperature, then rinsed again in PBT.

For preparation of adult eye samples, eyes were dissected in PBS and fixed with 3.7% formaldehyde-PBS for 30 mins. Fixed samples were washed three times in PBT (PBS with 0.4% Triton X-100) and kept at room temperature in PBT for up to 12 hrs to reduce the pigmentation of eyes. Samples were then incubated with 1:50 Alexa Fluor 633 phalloidin (A22284, ThermoFisher Scientific) for 2 hrs at room temperature and rinsed in PBT.

Antibodies

Primary antibody used for the first round is: mouse anti-Fasciclin II (DSHB, 1D4), 1:20. Conjugated secondary antibody used for the first round is: Goat anti-mouse Alexa-405 (A31553, Thermo Fisher Scientific), 1:250. Primary antibodies used for the second round are: mouse anti-Chaoptin (DSHB, 24B10), 1:20; Chicken anti-GFP (abcam, ab13970), 1:400; Rabbit anti-RFP (Rockland), 1:400. Conjugated secondary antibodies used for the second round are: Donkey anti-mouse Alexa-647 (A31571, Thermo Fisher Scientific), 1:100; Goat anti-chicken Alexa-488 (A32931, Thermo Fisher Scientific), 3:500; Donkey anti-rabbit Alexa-568 (A10042, Thermo Fisher Scientific), 1:500.

Mounting and Imaging

Samples were mounted in VECTASHIELD Antifade Mounting Medium. Samples were mounted so that the eye imaginal disk is on the top next to the cover slip, and the optic lobe is on the bottom. Images were obtained on a Nikon A1R-Si inverted confocal microscope with 4 line laser unit (405/488/561/640) and with a 60X oil objective. Z stacks were acquired with a step size of 0.125 μm between optical sections.

Image Processing for Visual Inspection and Figure Generation

Images were transformed from ND2 format to TIF format and background subtracted in batch using custom ImageJ macro script on a HPC cluster (code available on GitHub: https://github.com/AltschulerWu-Lab/nsp_extension).

To calculate the penetration of *sev>Fz* and *sev>N^{tc}* perturbation (Table 2-1), images of *sev>Fz* lamina samples at 38 hrs APF and *sev>N^{tc}* lamina samples at 45 hrs APF were visually inspected using Fiji (<http://fiji.sc/>) and targets of bundles with two R3s (bundles with two RFP-positive R cell growth cones and

no GFP-positive R cell growth cones) or two R4s (bundles with two GFP-positive R cell growth cones) are counted. Only bundles with R cell growth cones that can be easily traced from origin to target are included in the counting. Fz and N^{ic} perturbation were scored at different developmental time points due to the decay of quality of GFP signal in *sev>Fz* samples over time.

To generate representative images of bundle targeting phenotypes (Figure 2-1), we annotated cropped confocal images of *sev>Fz* samples at 38 hrs APF and *sev>N^{ic}* samples at 45 hrs APF in Amira 2020.1 (FEI Visualization Sciences Group). For each cropped image stack, growth cones from one bundle were manually segmented in both GFP and RFP channels. Segmented growth cones were then rendered with the appropriate color (red for RFP and green for GFP) in volume, and the unsegmented FasII channel was overlaid as an ortho-slice in grayscale. TIF files of the results were then exported from Amira and further annotated using Adobe Illustrator. To show bundles in consistent orientations, some images were rotated and/or flipped. Images were also cropped to highlight the representative bundle.

To generate representative images of bundles from 22 to 36 hrs APF (Figures 2-2, A-1, A-4), images of lamina samples were inspected and adjusted using Fiji (<http://fiji.sc/>). Brightness and contrast of individual channels were adjusted separately, and only one z-stack was selected for visualization purpose. Images are also cropped to highlight the representative bundle. Tiff files of individual channels were exported from Fiji and further annotated using Adobe Illustrator. To show bundles in consistent orientations, some images were rotated and/or flipped. Images were also cropped to highlight the representative bundle.

Image Quantification Using Standardized Coordinates

Pre-preprocessing

Images of laminae were transformed from ND2 format to TIF format and background subtracted in batch using a custom ImageJ macro script on a HPC cluster (code available on GitHub: https://github.com/AltschulerWu-Lab/nsp_extension).

Annotation

Images were visually inspected, cropped and annotated using Fiji (<http://fiji.sc/>). Due to the variation in mounting and sparseness of labeling, only images of the lamina plexus with large intact regions were further analyzed. Images were cropped (in all directions) to keep the part of the lamina plexus that had sparse-enough labeling of growth cones. These cropped images were then used to manually annotate the position of growth cone heels (starting positions) and targets. Heels of growth cones were annotated based on the 24B10 channel using the “Multi-point tool”, while targets were annotated based on the FasII channel using the “Elliptical selections” tool. Multiple z-slices were used to annotate target ellipses to better represent the boundaries of FasII staining. X, Y, positions of heels and major, minor axis lengths and the major axis angle of the target ellipse were exported to a csv file for later quantification. Mapping of each bundle number to its corresponding target numbers was also noted in another csv file. Bundles with rotational defects were not included in the annotation.

Quantification

Standardized coordinate system. We used custom Python scripts (code available on GitHub: https://github.com/AltschulerWu-Lab/nsp_extension) to resample GFP and RFP images of each bundle to obtain representative density maps according to a standardized coordinate. Our standardized coordinate system (see Figure 2-2) resembles a polar coordinate system. The center of the coordinate system ($C = (0,0)$) is defined as the intersection of the lines connecting R3 and T3 and R4 and T3'. The polar coordinate is normalized so that: 1) the radius $|C-T4| = 1$ (A.U.) and 2) the targets T3 and T3' are placed at angles +1 and -1 (A.U.), respectively. The centers of the target ellipses were used as reference points for the standardized coordinate system.

Density map of image slice. We converted image data to a density map in our standardized coordinates in two steps. First, we created a coordinate grid (the radius ranged from 0 to 3.8 with 0.05 intervals; the angles ranged from -3 to 3 with 0.05 intervals). Second, we used the N-dimensional piecewise linear interpolation function within the Python numpy package (v1.16.4) to create a map from Cartesian to

polar coordinates; this allowed us to convert GFP and RFP images into density maps in the new coordinate system.

Density map of bundle. Density maps for each bundle were computed using the mean density map across z-stacks containing 41 slices, which were centered around the z-slice showing the longest growth cone (typically R3 and/or R4). We manually annotated the length and angle of R3 or R4 growth cones of a given bundle according to the RFP or GFP density map, respectively. Length and angle of growth cones were annotated based on the longest filopodia in the front of the growth cone. Growth cones located in regions where GFP or RFP signals were too dense to distinguish the front were excluded from the annotation. If growth cones exhibit split morphology (i.e., two or more major long filopodia in the front), angles are calculated by the mean of these filopodia. Growth cones were labeled as R3 or R4 based on the absence or presence (respectively) of GFP signals.

Simulation of Repulsion Model

Heel and target positions were mapped to the standardized coordinate system. Simulated extension angles (\vec{v}_p) were calculated based on weighted vector sum of two vectors (\vec{v}_1, \vec{v}_2). For extension angles of R3, the repulsion vectors: \vec{v}_1 was taken to be the unit vector from the R2 to R3 heels; and \vec{v}_2 was taken to be the unit vector from the R4 to R3 heels. For extension angles of R4, the repulsion vectors: \vec{v}_1 was taken to be the unit vector from the R5 to R4 heels; and \vec{v}_2 was taken to be the unit vector from the R3 to R4 heels. The weight of each vector represented the strength of its repulsive force. For simple repulsion from neighboring heels, $\vec{v}_p = (\vec{v}_1 + \vec{v}_2)$. To estimate unequal influence of neighboring growth cone heels, linear regression was performed on $\vec{v}_p = \alpha \vec{v}_1 + \beta \vec{v}_2$ using pooled data from wild-type measurements between 22 to 26 hrs APF. Only data from bundles that were relatively symmetric in shape ($\frac{|\Delta(T3,C,T4) - \Delta(T3',C,T4)|}{\max\{\Delta(T3,C,T4), \Delta(T3',C,T4)\}} \leq 0.5$) were included in the regression analysis. R3 and R4 angles were fitted independently. Regression analysis was implemented in Python using the scikit-learn package (v0.23.2).

Statistical Analysis

Sample sizes for each experiment are provided in the figure legends. Statistics were computed in Python using the `scipy` (v1.2.1) and `scikit-posthocs` (v0.6.4) packages. A two-sided Mann-Whitney U test was applied when there were only two groups of data being compared. When there were more than two groups, we applied a Kruskal–Wallis H test followed by a post-hoc two-sided Mann-Whitney test with p values adjusted by Bonferroni method. The error bars displayed in all figures represent standard deviation of the mean.

References

1. Lichtman JW, Colman H. Synapse Elimination and Indelible Memory. *Neuron*. 2000;25(2):269–78.
2. Purves D. *Body and Brain: A Trophic Theory of Neural Connections*. Harvard University Press; 1988. 231 p.
3. Agi E, Kulkarni A, Hiesinger PR. Neuronal strategies for meeting the right partner during brain wiring. *Curr Opin Neurobiol*. 2020;63:1–8.
4. Langen M, Agi E, Altschuler DJ, Wu LF, Altschuler SJ, Hiesinger PR. The Developmental Rules of Neural Superposition in *Drosophila*. *Cell*. 2015;162(1):120–33.
5. Clandinin TR, Zipursky SL. Afferent Growth Cone Interactions Control Synaptic Specificity in the *Drosophila* Visual System. *Neuron*. 2000;28(2):427–36.
6. Chen P-L, Clandinin TR. The Cadherin Flamingo Mediates Level-Dependent Interactions that Guide Photoreceptor Target Choice in *Drosophila*. *Neuron*. 2008;58(1):26–33.
7. Schwabe T, Neuert H, Clandinin TR. A Network of Cadherin-Mediated Interactions Polarizes Growth Cones to Determine Targeting Specificity. *Cell*. 2013;154(2):351–64.
8. Strutt DI, Weber U, Mlodzik M. The role of RhoA in tissue polarity and Frizzled signalling. *Nature*. 1997;387(6630):292–5.
9. Zheng L, Zhang J, Carthew RW. frizzled regulates mirror-symmetric pattern formation in the *Drosophila* eye. *Dev Camb Engl*. 1995;121(9):3045–55.
10. Cooper MTD, Bray SJ. Frizzled regulation of Notch signalling polarizes cell fate in the *Drosophila* eye. *Nature*. 1999;397(6719):526–30.
11. Fanto M, Mlodzik M. Asymmetric Notch activation specifies photoreceptors R3 and R4 and planar polarity in the *Drosophila* eye. *Nature*. 1999;397(6719):523–6.
12. Bohm RA, Welch WP, Goodnight LK, Cox LW, Henry LG, Gunter TC, et al. A genetic mosaic approach for neural circuit mapping in *Drosophila*. *Proc National Acad Sci*. 2010;107(37):16378–83.
13. Chou TB, Perrimon N. The autosomal FLP-DFS technique for generating germline mosaics in *Drosophila melanogaster*. *Genetics*. 1996;144(4):1673–9.

14. Agi E, Langen M, Altschuler SJ, Wu LF, Zimmermann T, Hiesinger PR. The Evolution and Development of Neural Superposition. *J Neurogenet.* 2014;28(3–4):216–32.
15. Norden C, Lecaudey V. Collective cell migration: general themes and new paradigms. *Curr Opin Genet Dev.* 2019;57:54–60.
16. Reig G, Pulgar E, Concha ML. Cell migration: from tissue culture to embryos. *Development.* 2014;141(10):1999–2013.
17. Braitenberg V. Patterns of projection in the visual system of the fly. I. Retina-lamina projections. *Exp Brain Res.* 1967;3(3):271–98.
18. Horridge GA, Meinertzhagen IA. The accuracy of the patterns of connexions of the first- and second-order neurons of the visual system of Calliphora. *Proc Royal Soc Lond Ser B Biological Sci.* 1970;175(1038):69–82.
19. Meinertzhagen IA. Erroneous projection of retinula axons beneath a dislocation in the retinal equator of Calliphora. *Brain Res.* 1972;41(1):39–49.
20. Hiesinger PR, Zhai RG, Zhou Y, Koh T-W, Mehta SQ, Schulze KL, et al. Activity-Independent Preshpecification of Synaptic Partners in the Visual Map of Drosophila. *Curr Biol.* 2006;16(18):1835–43.
21. Matsubara D, Horiuchi S, Shimono K, Usui T, Uemura T. The seven-pass transmembrane cadherin Flamingo controls dendritic self-avoidance via its binding to a LIM domain protein, Espinas, in Drosophila sensory neurons. *Gene Dev.* 2011;25(18):1982–96.
22. Senti K-A, Usui T, Boucke K, Greber U, Uemura T, Dickson BJ. Flamingo Regulates R8 Axon-Axon and Axon-Target Interactions in the Drosophila Visual System. *Curr Biol.* 2003;13(10):828–32.
23. Dent EW, Gupton SL, Gertler FB. The Growth Cone Cytoskeleton in Axon Outgrowth and Guidance. *Csh Perspect Biol.* 2011;3(3):a001800.
24. Geraldo S, Gordon-Weeks PR. Cytoskeletal dynamics in growth-cone steering. *J Cell Sci.* 2009;122(20):3595–604.
25. Berezovska O, McLean P, Knowles R, Frosh M, Lu FM, Lux SE, et al. Notch1 inhibits neurite outgrowth in postmitotic primary neurons. *Neuroscience.* 1999;93(2):433–9.

26. Franklin JL, Berechid BE, Cutting FB, Presente A, Chambers CB, Foltz DR, et al. Autonomous and non-autonomous regulation of mammalian neurite development by Notch1 and Delta1. *Curr Biol*. 1999;9(24):1448–57.
27. Šestan N, Artavanis-Tsakonas S, Rakic P. Contact-Dependent Inhibition of Cortical Neurite Growth Mediated by Notch Signaling. *Science*. 1999;286(5440):741–6.
28. Ferrari-Toninelli G, Bonini SA, Bettinsoli P, Uberti D, Memo M. Microtubule stabilizing effect of notch activation in primary cortical neurons. *Neuroscience*. 2008;154(3):946–52.
29. Ferrari-Toninelli G, Bonini SA, Uberti D, Napolitano F, Stante M, Santoro F, et al. Notch activation induces neurite remodeling and functional modifications in SH-SY5Y neuronal cells. *Dev Neurobiol*. 2009;69(6):378–91.
30. Özel MN, Kulkarni A, Hasan A, Brummer J, Moldenhauer M, Daumann I-M, et al. Serial Synapse Formation through Filopodial Competition for Synaptic Seeding Factors. *Dev Cell*. 2019;50(4):447-461.e8.
31. Purves D, Lichtman J. Elimination of synapses in the developing nervous system. *Science*. 1980;210(4466):153–7.
32. Katz LC, Shatz CJ. Synaptic Activity and the Construction of Cortical Circuits. *Science*. 1996;274(5290):1133–8.
33. Hashimoto K, Kano M. Functional Differentiation of Multiple Climbing Fiber Inputs during Synapse Elimination in the Developing Cerebellum. *Neuron*. 2003;38(5):785–96.
34. Hashimoto K, Kano M. Postnatal development and synapse elimination of climbing fiber to Purkinje cell projection in the cerebellum. *Neurosci Res*. 2005;53(3):221–8.
35. Godement P, Wang L, Mason C. Retinal axon divergence in the optic chiasm: dynamics of growth cone behavior at the midline [published erratum appears in *J Neurosci* 1995 Mar;15(3):following table of contents]. *J Neurosci*. 1994;14(11):7024–39.
36. Hutson LD, Chien C-B. Wiring the zebrafish: axon guidance and synaptogenesis. *Curr Opin Neurobiol*. 2002;12(1):87–92.

37. Bak M, Fraser SE. Axon fasciculation and differences in midline kinetics between pioneer and follower axons within commissural fascicles. *Development*. 2003;130(20):4999–5008.
38. Jontes JD, Buchanan J, Smith SJ. Growth cone and dendrite dynamics in zebrafish embryos: early events in synaptogenesis imaged in vivo. *Nat Neurosci*. 2000;3(3):231–7.
39. Hedgecock EM, Culotti JG, Hall DH. The *unc-5*, *unc-6*, and *unc-40* genes guide circumferential migrations of pioneer axons and mesodermal cells on the epidermis in *C. elegans*. *Neuron*. 1990;4(1):61–85.
40. Wadsworth WG, Bhatt H, Hedgecock EM. Neuroglia and Pioneer Neurons Express UNC-6 to Provide Global and Local Netrin Cues for Guiding Migrations in *C. elegans*. *Neuron*. 1996;16(1):35–46.

Appendix A - Supplemental Material for Chapter 2

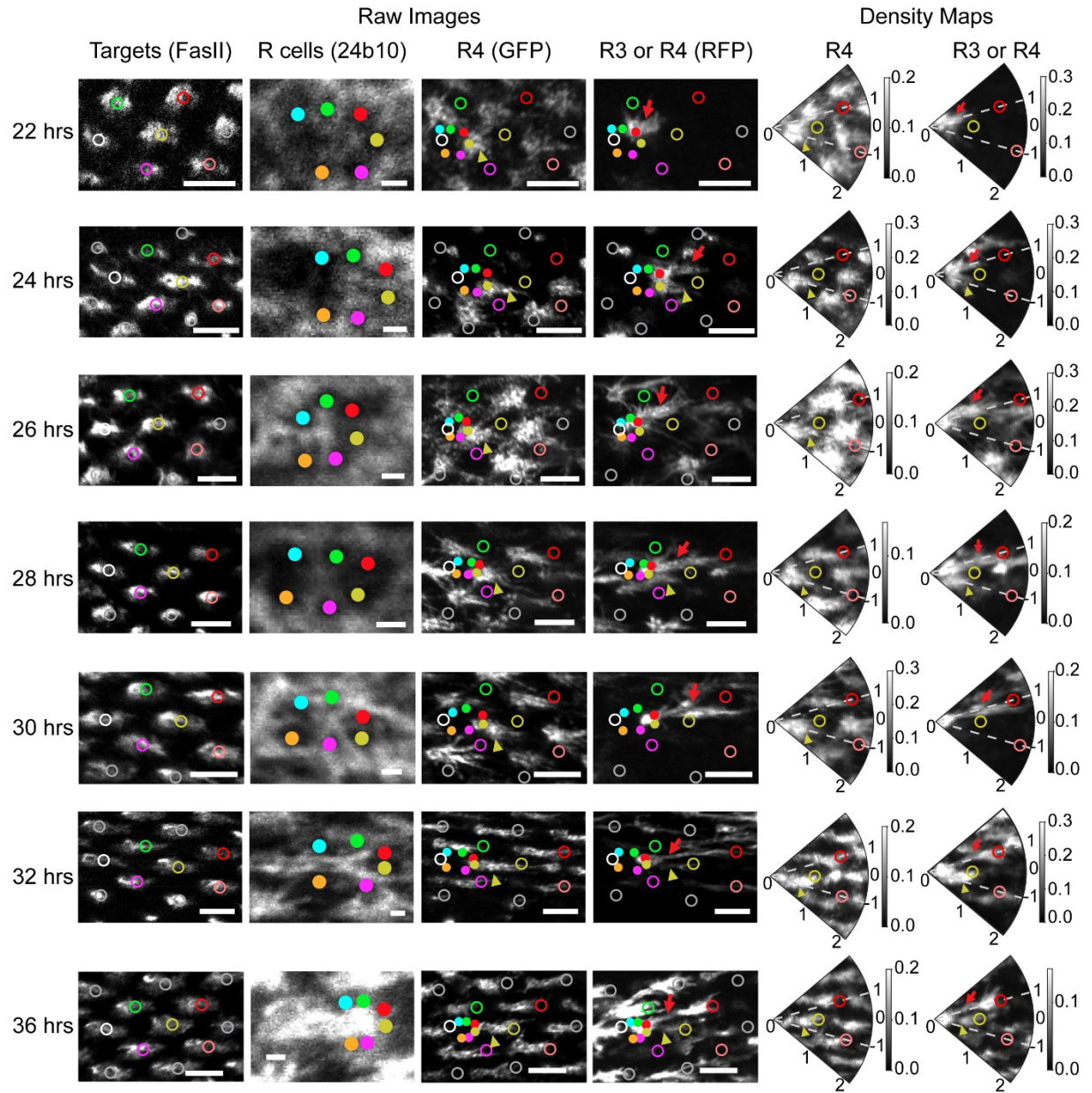


Figure A-1: Extension phenotype of wild-type flies over time.

Representative images of bundles from wild-type flies from 22 to 36 hrs APF. Left: Raw images of example bundles. From left to right: FasII channel labeling the target cells; 24B10 channel labeling membrane of all R cells; GFP channel labeling membrane of R4 cells; RFP channel labeling membrane of R3 or R4 cells. Right: Density maps of GFP (R4 cells) and RFP channel (R3 or R4 cells) after coordinate transformation. For visualization, intensity is scaled differently for each channel and for each sample. R-cells and targets indicated and colored as in Figure 2-1; white circles: T0; gray circles: other targets. Yellow arrowheads: R4 growth cones; red arrows: R3 growth cones. Scale bars: 5 μm for FasII, GFP and RFP images; 1 μm for 24B10 images.

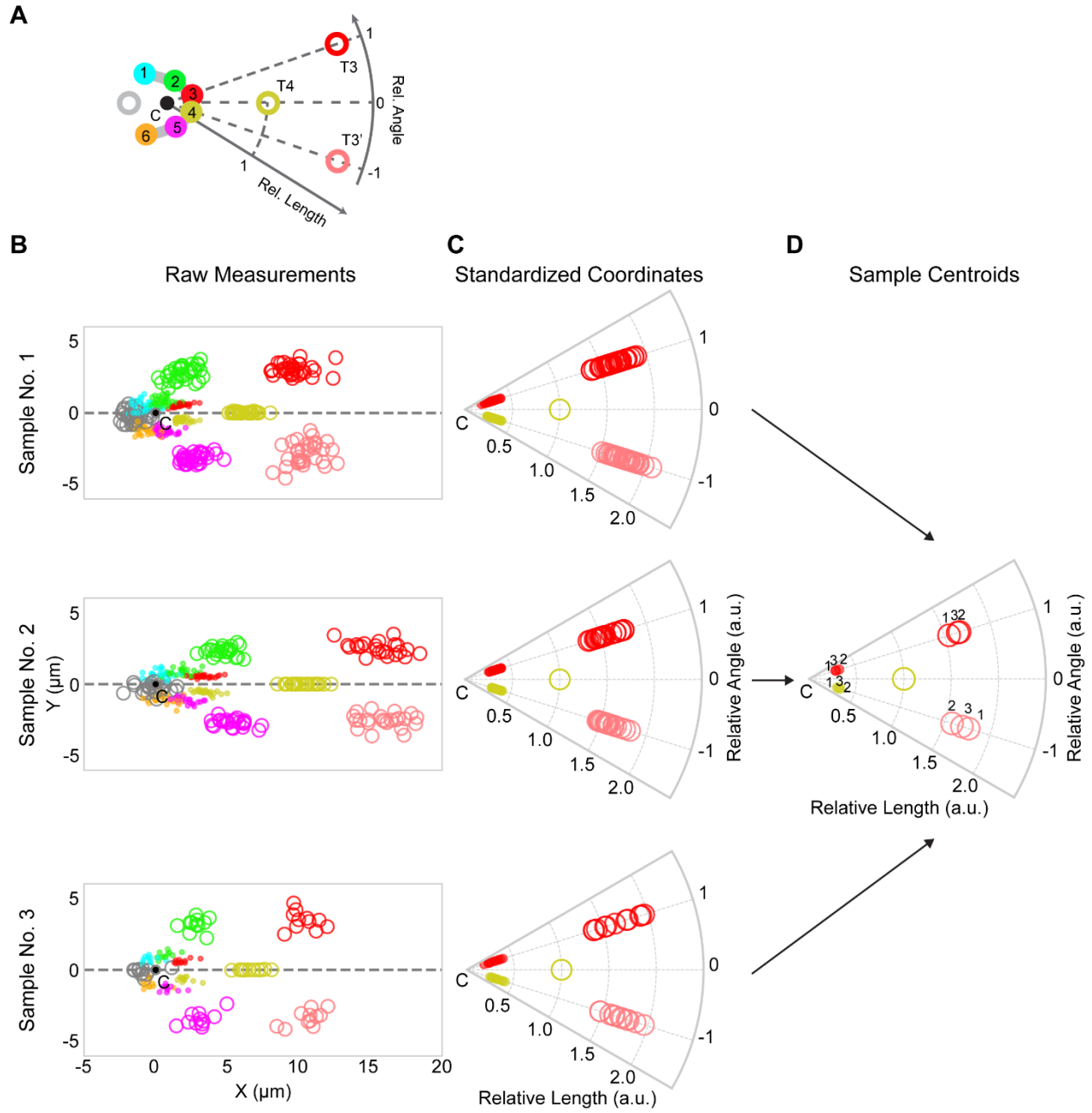


Figure A-2: Variation of the standardized coordinate system across samples.

(A) Schematic of the standardized coordinate system. (B) Shown are the raw heel (filled circle) and target (hollow circle) grids for each bundle in three different samples (taken from wild-type at 26hrs APF) aligned so that the “C” point (center of the standardized coordinate) is at (0,0) and T4 is on the X-axis. (C) Raw data for samples 1-3 in (B) are transformed so that $|C-T4| = 1$ and $\angle(T3,C,T4) = \angle(T4,C,T3') = 1$. Only data relevant to R3 and R4 are shown. (D) Centroids for samples 1-3 in (C) are shown.

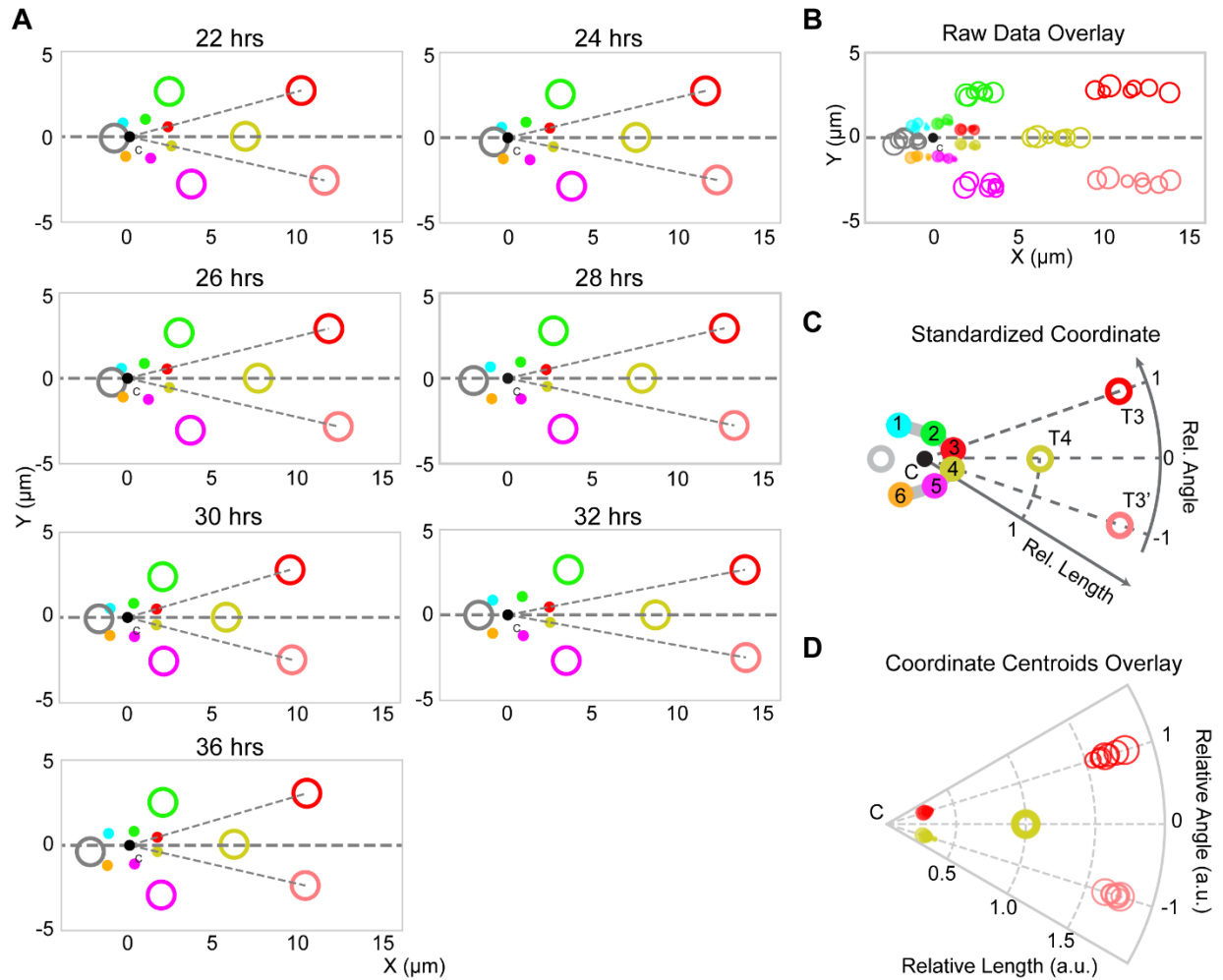


Figure A-3: Variation of the standardized coordinate system across time points.

(A) Centroid of aligned heel and target positions of all bundles at given time points. Alignment is the same as Figure A-2. (B) Alignment of all centroids across time points. (C) Schematic of the standardized coordinate system. (D) Polar plot of centroid of standardized coordinates across time points. Increasing circle size indicates progression in time.

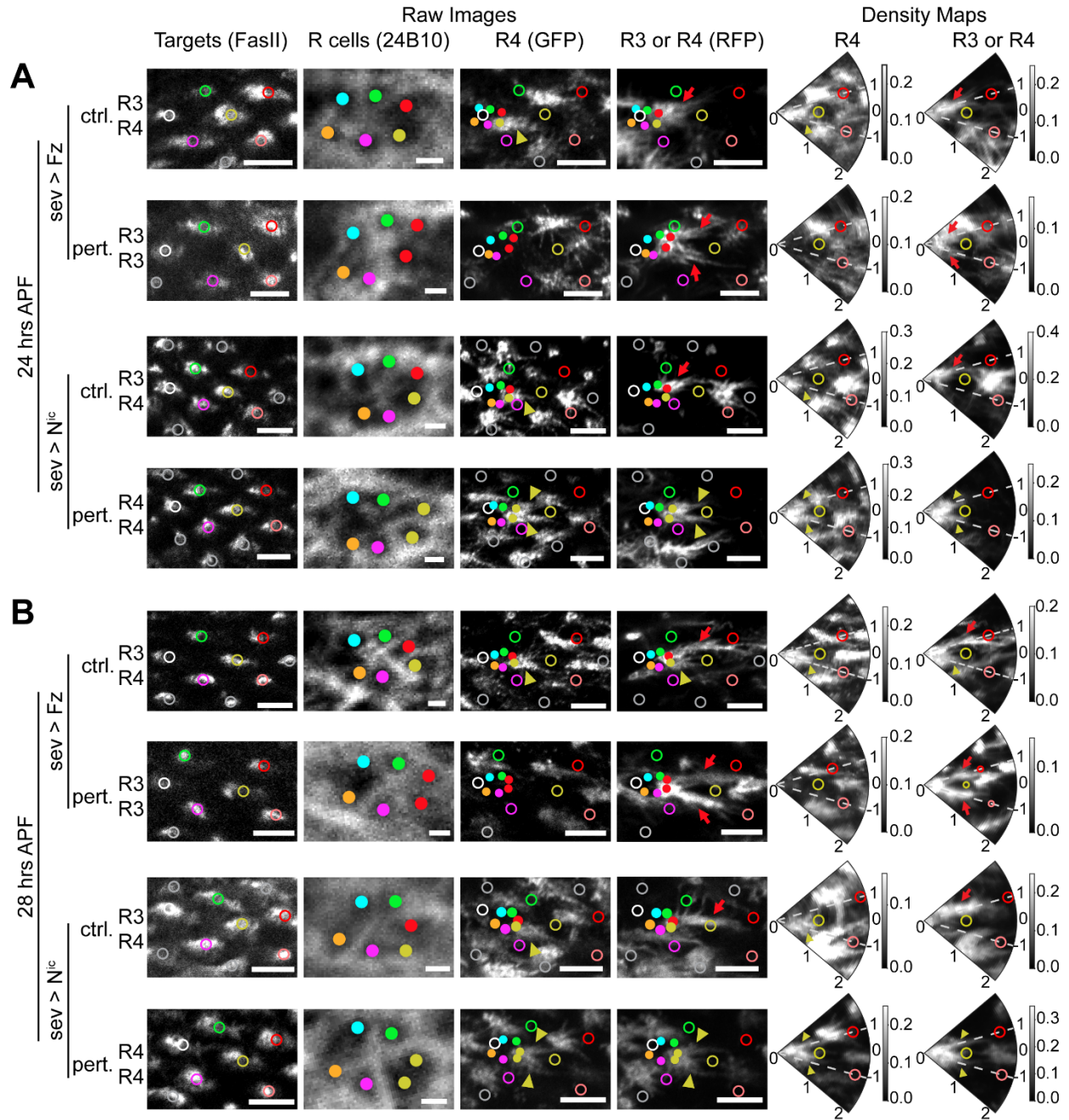


Figure A-4: Extension phenotype of *sev>Fz* and *sev>N^{ic}* flies over time.

(A-B) Representative images of wild-type-like (ctrl.) and fate-transformed (pert.) bundles in *sev>Fz* and *sev>N^{ic}* flies at (A) 24 or (B) 28 hrs APF. Left four panes are confocal images of example bundles. Right two panels are density maps of GFP (R4 cells) and RFP channel (R3 or R4 cells) after coordinate transformation. Image channels, intensity normalization, annotation and scale bars are as in Figure A-1.

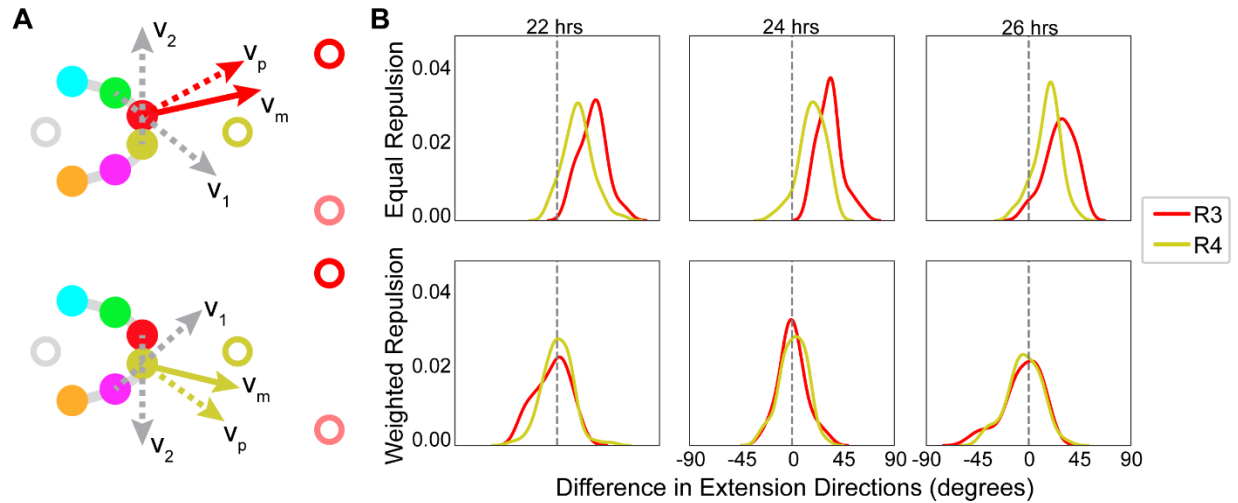


Figure A-5: Repulsion model for determining growth cone extension angle.

(A) Schematics of repulsion model. For R3, \vec{v}_1 and \vec{v}_2 represent repulsive forces from R2 and R4, respectively. For R4, \vec{v}_1 and \vec{v}_2 represent repulsive forces from R5 and R3, respectively. \vec{v}_p : extension direction predicted from simulation; \vec{v}_m : extension direction measured. (B) Difference between predicted and actual extension directions for data from 22, 24 or 26 hrs APF. $\vec{v}_p = \alpha \vec{v}_1 + \beta \vec{v}_2$ is used to calculate predicted extension directions. For the equal repulsion model, $\alpha = \beta = 0.5$. For the weighted repulsion model, linear regression is performed to get α and β that best fit pooled data from wild-type measurements between 22 to 26 hrs APF. R3 regression result: $\alpha = 1.04$, $\beta = 0.44$, $R^2 = 0.76$; R4 regression result: $\alpha = 1.00$, $\beta = 0.64$, $R^2 = 0.88$.

Table A-1: P-values for data used to create Figure 2-3.

For Figure 2-3A, significance is calculated using the two-sided Mann-Whitney test with p values adjusted by Bonferroni method. For Figure 2-3B, significance is calculated using the two-sided Mann-Whitney test.

Related Figure Number	Sample Genotype	Data Category	p values	
Figure 2-3A	wild-type	Relative length of R3s	22 vs. 24 hrs	1
			24 vs. 26 hrs	1.84×10^{-5}
			26 vs. 28 hrs	4.67×10^{-6}
			28 vs. 30 hrs	0.529
			30 vs. 32 hrs	0.529
			32 vs. 36 hrs	0.006
		Relative length of R4s	22 vs. 24 hrs	0.737
			24 vs. 26 hrs	8.70×10^{-4}
			26 vs. 28 hrs	1
			28 vs. 30 hrs	0.057
			30 vs. 32 hrs	1.0
			32 vs. 36 hrs	1.0
Figure 2-3B		Relative Angle of R3s and R4s	22 hrs, R3 vs. R4	0.165
			24 hrs, R3 vs. R4	0.489
			26 hrs, R3 vs. R4	0.063
			28 hrs, R3 vs. R4	0.057
			30 hrs, R3 vs. R4	0.002
			32 hrs, R3 vs. R4	4.20×10^{-10}
			36 hrs, R3 vs. R4	1.10×10^{-11}

Table A-2: P-values for data used to create Figure 2-4.

Significance is calculated using the two-sided Mann-Whitney test with p values adjusted by Bonferroni method. ctrl.: wild-type-like bundles; pert.: perturbed bundles; pos. R3: growth cone at R3 position; pos. R4: growth cone at R4 position.

Related Figure Number	Sample Genotype	Data Category	p-values	
Figure 2-4A	sev>Fz, 24hrs	Relative length	ctrl. pos. R3 vs. ctrl. pos. R4	0.004
			pert. pos. R3 vs. pert. pos. R4	1.0
			ctrl. pos. R3 vs. pert. pos. R3	1.0
			ctrl. pos. R3 vs. ctrl. pos. R4	1.0
		Relative angle	ctrl. pos. R3 vs. ctrl. pos. R4	1.0
			pert. pos. R3 vs. pert. pos. R4	1.0
			ctrl. pos. R3 vs. pert. pos. R3	1.0
			ctrl. pos. R4 vs. pert. pos. R4	0.372
	sev>Fz, 28hrs	Relative length	ctrl. pos. R3 vs. ctrl. pos. R4	5.77×10^{-25}
			pert. pos. R3 vs. pert. pos. R4	1.0
			ctrl. pos. R3 vs. pert. pos. R3	1.0
			ctrl. pos. R3 vs. ctrl. pos. R4	0.839
		Relative angle	ctrl. pos. R3 vs. ctrl. pos. R4	0.139
			pert. pos. R3 vs. pert. pos. R4	1.0
			ctrl. pos. R3 vs. pert. pos. R3	1.0
			ctrl. pos. R4 vs. pert. pos. R4	0.664
Figure 2-4B	sev>N ^{ic} , 24 hrs	Relative length	ctrl. pos. R3 vs. ctrl. pos. R4	6.00×10^{-6}
			pert. pos. R3 vs. pert. pos. R4	1.0
			ctrl. pos. R4 vs. pert. pos. R3	1.0
			ctrl. pos. R4 vs. pert. pos. R4	1.0
		Relative angle	ctrl. pos. R3 vs. ctrl. pos. R4	0.067
			pert. pos. R3 vs. pert. pos. R4	1.0
			ctrl. pos. R3 vs. pert. pos. R3	1.0
			ctrl. pos. R4 vs. pert. pos. R4	1.0
	sev>N ^{ic} , 28hrs	Relative length	ctrl. pos. R3 vs. ctrl. pos. R4	6.30×10^{-18}
			pert. pos. R3 vs. pert. pos. R4	1.0
			ctrl. pos. R4 vs. pert. pos. R3	1.0
			ctrl. pos. R4 vs. pert. pos. R4	1.0
		Relative angle	ctrl. pos. R3 vs. ctrl. pos. R4	0.825
			pert. pos. R3 vs. pert. pos. R4	1.0
			ctrl. pos. R3 vs. pert. pos. R3	1.0
			ctrl. pos. R4 vs. pert. pos. R4	1.0

Publishing Agreement

It is the policy of the University to encourage open access and broad distribution of all theses, dissertations, and manuscripts. The Graduate Division will facilitate the distribution of UCSF theses, dissertations, and manuscripts to the UCSF Library for open access and distribution. UCSF will make such theses, dissertations, and manuscripts accessible to the public and will take reasonable steps to preserve these works in perpetuity.

I hereby grant the non-exclusive, perpetual right to The Regents of the University of California to reproduce, publicly display, distribute, preserve, and publish copies of my thesis, dissertation, or manuscript in any form or media, now existing or later derived, including access online for teaching, research, and public service purposes.

DocuSigned by:

2A85DA65DD77470... Author Signature

9/2/2021
Date